Chorus intensification in response to interplanetary shock: THEMIS observations

H. S. Fu[1, 2, 5], J. B. Cao[1], F. S. Mozer[3], H. Y. Lu[1], B. Yang[4]

[1]Space Science Institute, School of Astronautics, Beihang University, Beijing 100191, China

[2]Swedish Institute of Space Physics, Uppsala, Sweden

[3]Space Sciences Laboratory, University of California, Berkeley, CA 94720, USA

[4]Institute of Space Physics and Applied Technology, Peking University, Beijing 100871, China

[5]State Key Laboratory for Space Weather/CSSAR, Beijing, China

Abstract.

On 3 September 2009, the Time History of Events and Macroscale Interactions during Substorms (THEMIS) satellites observed a significant intensification of chorus in response to the interplanetary shock in the Earth's dayside plasmatrough. We analyze the wave-particle interaction and reveal that the chorus intensification can be caused by the gyro-resonance between the chorus and the energetic electrons. When the electrons are scattered from resonance points to low-density region along the diffusion curves, a part of their energy can be lost and then transferred to amplify the chorus. During the compression of magnetosphere, the temperature anisotropy of electrons is enhanced. This makes the electron diffusion and chorus intensification very effective. The maximum growth rate after the shock is about 50% greater than that before the shock. The lower-energy (15 - 25 keV) electrons contribute more to the growth of chorus due to the larger density gradient along the diffusion curve. The < 10 keV electrons are almost isotropic so they contribute little to the amplification of chorus. We investigate the free energy for the chorus intensification and find that it can be generated through the local betatron acceleration and radial diffusion processes. The local betatron acceleration results from the shock-induced compression of magnetosphere. The linear and nonlinear growth rates are also compared. We find the linear diffusion process works well for the present case.

1. Introduction

On the Earth's morning side, a type of electromagnetic emission in the audio frequency range can usually be received by the instrument [*Oliven and Gurnett*, 1968]. It sounds much like the bird chirps when played through a loud speaker and is thus named as chorus [e.g., *Burtis and Helliwell*, 1969; *Rodger and Clilverd*, 2008]. Chorus consists of discrete elements with rising or falling tones in the frequency-time spectrogram [e.g., *Omura et al.,* 1991; *Sazhin and Hayakawa*, 1992, and references therein]. They appear usually as two bands in the plasmatrough region: a lower band in the range from 0.1 to 0.45 f_{ce}, and an upper band in the range from 0.5 to 0.7 f_{ce}, where f_{ce} represents the equatorial gyro-frequency of electrons. The absence of chorus near 0.5 f_{ce} is suggested to result from the Landau damping [e.g., *Li et al.,* 2010]. Chorus is usually generated on the equatorial plane and then propagates along the geomagnetic field line to mid-latitude. During the propagation process of chorus, the nonlinear wave-particle interaction may be very important since the electrons can be trapped by the wave electric field [e.g., *Omura and Summers*, 2006; *Omura et al.,* 2009]. The characteristics of chorus in the source region have been investigated by *Santolík et al.* [2003; 2004]. Near the equatorial plane, chorus has a transversal dimension of 7-100 km [*Santolík and Gurnett*, 2003]. Based on the POLAR data, *Bunch et al.* [2011] show the statistical distribution of chorus wave power in the off□equatorial region. Recently, the THEMIS observations reveal that the chorus can be well modulated by both the Pc4-5 pulsations [*Li et al.,* 2011a] and the plasma density [*Li et al.,* 2011b]. The variation of plasma density can lead to the change of wave-particle resonance conditions. Some statistical studies indicated that chorus is correlated with the interplanetary shock [e.g., *Gail et al.,* 1990*; Gail and Inan,* 1990*;*

Lauben et al., 1998] and the disturbing geomagnetic condition [e.g., *Meredith et al.*, 2001; 2003; *Miyoshi et al.*, 2003; *Lyons et al.*, 2005; *Cao et al.*, 2007; *Yang et al.*, 2007; 2008].

Chorus receives increasing attentions recently due to its key role in accelerating electrons to relativistic energies [*Horne et al.*, 2005a] in the outer radiation belt [*Baker et al.*, 2004], which produces a disastrous space environment for humans and spacecraft. In addition, chorus can also be responsible for the source of hiss [e.g., *Bortnik et al.*, 2008; 2009] and the diffuse aurora in the polar region [e.g., *Nishimura et al.*, 2010; *Thorne et al.*, 2010]. Although chorus is very important and has been studied for several decades, its generation and growth process are still not well understood [*Li et al.,* 2009]. A widely accepted mechanism is the gyro-resonance [e.g., *Burton and Holzer*, 1974; *Helliwell*, 1967; *Tsurutani and Smith*, 1977], which has been studied for many years with different models and simulation methods. For instance, by solving the Maxwell's equations together with the electron fluid equation for the cold dense electrons and the motion equations for the hot resonant electrons, *Katoh and Omura* [2006, 2007a, 2007b] successfully reproduced the main feature of the chorus in their simulations. *Omura and Summers* [2006] pointed out that the electromagnetic electron hole in the wave-phase-space is crucial for the growth of chorus because it can lead to a transverse resonant current. The backward wave oscillator (BWO) model, which assumes a step□like velocity distribution of energetic electrons, was also used to understand the generation of chorus [e.g., *Trakhtengerts,* 1995; *Kozelov et al.,* 2008].

By analyzing the experimental data, the generation and amplification of chorus have also been studied recently. The relationship between the wave amplitude and the sweep

rate of chorus elements was examined by *Cully et al.* [2011]. *Li et al.* [2008; 2009] observed an amplification of chorus in the nightside plasmatrough region. They attributed the chorus intensification to the energetic electrons injected from the plasma sheet.

In this study, we show another energy sources for the chorus intensification. We find that both radial diffusion and local betatron acceleration of electrons, which is induced by the interplanetary shock, can provide free energies for the chorus growth. We show an observational evidence of the chorus intensification as a consequence of gyro-resonance. We organize the paper as follows. Section 2 introduces the data and instruments used in this study. Section 3 presents the THEMIS observations of chorus intensification. In section 4, we analyze the wave-particle interaction process, and then section 5 discusses the energy sources. In section 6, the summary and conclusions of our study are presented. A discussion about the observation and wave-particle interaction is given in section 7.

2. Data and instrumentation

THEMIS is a multi-satellite mission launched on February 17, 2007 and is aimed at determining the evolution of substorms and the dynamics of energetic particles in the radiation belts [*Angelopoulos*, 2008]. Both the particle and wave instruments are equipped onboard the satellites. In this study, we use the data from the Electric Field Instruments (EFI), Search Coil Magnetometers (SCM), Fluxgate Magnetometers (FGM), Electrostatic Analyzers (ESA), and also the Solid State Telescopes (SST). EFI measures the electric field from DC up to 8 kHz [*Bonnell et al.*, 2008]. Six antennas are involved in the EFI measurement. Each of them also provides the on-board and ground-based estimation of spacecraft floating potential, which can be used to calculate the plasma

density if combined with the ESA data [*McFadden et al.*, 2008b; *Fu et al.*, 2011a]. SCM measures the magnetic field fluctuations from 0.1 Hz to 4 kHz [*Roux et al.*, 2008]. The measurements of EFI and SCM usually cover the range of chorus especially in the outer plasmatrough region where the equatorial gyro-frequency of electrons is considerably small. The wave amplitude measured by EFI and SCM has been calibrated according to the frequency response characteristics [*Bonnell et al.*, 2008]. In the normal mode, the filter bank (FBK) data can be used to display the characteristics of chorus; while in the burst mode, the high-resolution EFI and SCM data will be used directly. FGM measures the background magnetic field and its low frequency fluctuations (up to 64 Hz) in the near-Earth space [*Auster et al.*, 2008]. It covers the range of Pc4 (7-22 mHz) and Pc5 (2-7 mHz) pulsations that have been suggested to corelate with the radial diffusion process [e.g., *Throne*, 2010; *Su et al.*, 2011; *Fu et al.*, 2011a]. ESA and SST are the thermal particle analyzers. ESA measures the electron distribution functions over the energy range from about 10 eV up to 25 keV [*McFadden et al.*, 2008a]. SST measures the electron distribution functions in the energy range from ~30 keV to ~4 MeV [*Angelopoulos*, 2008]. In this study, however, only the measurements of the <80 keV electrons are considered. There is usually a systemic jump between the electron differential energy fluxes (dEFs) measured by ESA and SST. To remove this jump, we use the kappa distribution and relativistic kappa-type distribution [*Xiao et al.*, 2008] to fit the dEFs.

Figure 1 presents two examples of the fitting on 3 September 2009. One is at the quiet time (1551:06 UT), while the other is during the compression of magnetosphere (1551:15 UT). Both of them are used to analyze the wave-particle interaction in this

study. In Figures 1a and 1c, the dEFs before fitting are shown; In Figure 1b and 1d, the dEFs after fitting are shown. The color lines represent the dEFs over the pitch angle from α=0 to α=180° (34 in total). Among them, the black, green, and red lines represent, respectively, the dEFs at α=0, α=90°, and α=180°. We see that, at 1551:06 UT, these three components are almost the same; while at 1551:15 UT, the perpendicular component are much larger than the parallel/anti-parallel component especially for the > 15 keV electrons. The dEFs of the <25 keV electrons are measured by ESA, while the dEFs of the >30 keV electrons are measured by SST. A data jump is clearly seen between the ESA and SST measurements (shadow region). We elevate the dEFs measured by SST to some degree to remove this systemic jump. The kappa distribution

$$f(p)=\frac{\Gamma(\kappa+1)}{(2\pi)^{3/2}\theta^3\kappa^{3/2}\Gamma(\kappa-1/2)}\left[1+\frac{p^2}{2\kappa\theta^2}\right]^{-(\kappa+1)} \quad (1)$$

and relativistic kappa-type distribution [*Xiao et al.*, 2008]

$$f(p)=\frac{N}{4\pi I}\left[1+\frac{\sqrt{1+p^2}-1}{\kappa\theta^2}\right]^{-(\kappa+1)} \quad (2)$$

with parameters $\kappa=5$ and $\theta^2=0.01$ are considered during the elevation. In Figure 1b, we find the dEFs after calibration can basically follow these two types of distribution (thick blue and black lines), and the systemic jump is not clear. In Figure 1d, we find the parallel and anti-parallel components of dEFs can follow the kappa and relativistic kappa-type distribution. The perpendicular component, however, does not follow very well. This is reasonable because during the compression of magnetosphere the electrons are not in the equilibrium state. Since the kappa and relativistic kappa-type distribution have

been successfully used to fit the energetic electron fluxes in the inner magnetosphere [e.g., *Xiao et al.,* 2008], the fitting of dEFs in this case should be reasonable.

THEMIS consists of five satellites, however, only THEMIS A (ThA), D (ThD), and E (ThE) are considered in this study because they are located inside the magnetosphere and are able to observe the whistler mode chorus. Figure 2 shows the location of ThA (red squares), ThD (black triangles) and ThE (blue dots) at 1550 UT on 3 September 2009. As can be seen, the three satellites are close to each other. They are located in the dayside magnetosphere (Figure 2a) and near the equatorial plane (Figure 2b-2c). Therefore they may be near the source region of chorus [e.g., *Santolík and Gurnett*, 2003]. Since these satellites are also close to the subsolar point of the magnetopause (Figure 2d), they should be sensitive to the compression of magnetosphere. In Figure 2a, 2b and 2d, we notice that the *Xgsm* value of ThD is slightly larger than that of ThA and ThE. This means ThD may respond first to the compression of magnetosphere.

3. Chorus intensification

The solar wind and IMF conditions during the period 1000 – 2000 UT on 3 September 2009 are examined in Figure 3. From top to bottom, the solar wind density (a), solar wind velocity (b), *IMF Bz* (c), and solar wind dynamic pressure (d) are displayed respectively. As can be seen, in the early time (1000 - 1500 UT) of September 3, the solar wind and IMF conditions are very quiet. While at 1551 UT (vertical dashed line), the sudden enhancement of solar wind density (N_{sw}, from 5 cm^{-3} to 15 cm^{-3}), solar wind velocity (V_{sw}, 325 km/s to 380 km/s), Z-component of the interplanetary magnetic field (*IMF Bz*, 0 nT to 4 nT), and the solar wind dynamic pressure (P_{sw}, 1 nPa to 4.5 nPa) are

observed. This is the typical feature of an interplanetary shock [e.g., *Zong et al.*, 2009; *Fu et al.*, 2011c]. The enhanced solar wind dynamic pressure may compress the Earth's magnetosphere and then lead to the increase of magnetic field strength.

The whistler-mode chorus in the magnetosphere has a response to this interplanetary shock. Figure 4 exhibits the VLF waves (a, c, e) and background magnetic field (b, d, f) during the period from 1548 to 1553 UT on September 3. They are observed, respectively, by ThA (Figure 4a-4b), ThD (Figure 4c-4d) and ThE (Figure 4e-4f). Since the wave power spectrograms are derived from the FBK data, they have a low resolution. The three dashed white lines in each spectrogram represent, from top to bottom, f_{ce}, 0.45 f_{ce} and 0.1 f_{ce}, where f_{ce} is the equatorial gyro-frequency of electrons. Labeled below the abscissa is the orbital information of each satellite including the universe time (UT), L value, magnetic local time (MLT), magnetic latitude (MLAT), and the radial distance to the center of the Earth (r) in the unit of R_E. Here the L value is defined as the distance from the center of the Earth to the point where a magnetic field line crosses the equatorial plane. The T89 and IGRF model of magnetic field are used to trace the location of spacecraft to the equatorial plane to get this L value. We find from the orbital information that ThD and ThE are close to the equatorial plane (MLAT≈-11°), while ThA is slightly far away from the equatorial plane (MLAT≈-16°). The L value of spacecraft approximately equals to the radial distance (r) during this period. All three satellites observed intensive wave activities between 0.1 f_{ce} and 0.7 f_{ce}. These waves may be just the whistler-mode choruses. Before 1551 UT, the measured magnetic field strength is almost a constant. They are, respectively, ~50 nT (ThA), ~49 nT (ThD) and ~53 nT (ThE). However, at ~1551 UT, the interplanetary shock hits the Earth's magnetopause

and then compresses the magnetosphere. It causes the magnetic field strength to increase very quickly to ~56 nT (ThA), ~54 nT (ThD) and ~59 nT (ThE). This compression of magnetosphere lasts for ~20 s (see the shadow region in each panel). The choruses are amplified significantly in response to this compression at ~1551:15 UT (ThA), ~1551:13 UT (ThD) and ~1551:17 UT (ThE) (see the vertical line in each panel). The chorus intensification observed by ThD is earlier than that observed by ThA and ThE. This is due to the larger *Xgsm* value of ThD (see Figure 2d). After 1553 UT, the three THEMIS satellites are exposed in the magnetosheath because the magnetopause has pushed inward by the interplanetary shock (not shown).

During this period, ThE works in the particle burst mode hence can provide high-resolution data of SCM. Figure 5 displays the measurements of SCM axis 2 (a) and axis 3 (b) from 1550:30 to 1552:00 UT. The three white solid lines represent, similarly, the equatorial gyro-frequency f_{ce}, 0.45 f_{ce} and 0.1 f_{ce} from top to bottom. The blue dotted lines express the plasma density derived from the spacecraft potential by applying the formula [e.g., *Pedersen et al*. 2008; *Fu et al.*, 2011a],

$$N_e = ae^{-\frac{\varphi}{b}} + ce^{-\frac{\varphi}{d}} \qquad (3)$$

where φ represents the sum of the spacecraft potential and the bias potential, and N_e is the plasma density. Parameters are set as a=c=0.023, b=d=2.0 in this case after considering the calibration with strong convection flows [e.g., *McFadden et al.,* 2008b; *Fu et al.*, 2011a]. We can see two bands of whistlers in these spectrograms. One is from 0.1 to 0.45 f_{ce}, and the other from 0.5 to 0.7 f_{ce}. The lower band is more intense than the upper band, and a gap is observed around 0.5 f_{ce}. All these characteristics satisfy the definition of

chorus. The rising or falling tones are not observed in these spectrograms probably due to that the data resolution (1 s) is not high enough. We can see that, before 1551:15 UT, the choruses are relatively weak; while after 1551:17 UT (vertical line), the choruses are amplified significantly. The average amplitude of the lower-band (0.1-0.45 f_{ce}) chorus at 1551:14 UT is ~5.0×10^{-7} nT^2/Hz, while at 1551:18 UT, it is ~4.8×10^{-6} nT^2/Hz. They are corresponding to 14 dB (1551:14 UT) and 34 dB (1551:18 UT) with respect to 10^{-7} nT^2/Hz. This means the choruses can be amplified 20 dB during the compression of magnetosphere. These amplified choruses exist from 1551:17 to 1551:28 UT. After 1551:28 UT, the choruses are damped. We suggest that the chorus intensification at 1551:17 UT can be explained as a response to the interplanetary shock (see also Figure 4e-4f). The plasma density decreases from 5.8 cm^{-3} (1551:13 UT) to 4.2 cm^{-3} (1551:45 UT), making the sum of thermal pressure and magnetic pressure always a constant. The frequency of chorus is slightly elevated after 1551:17 UT due to the enhanced magnetic field.

4. Chorus – electron interaction

To examine whether the seed chorus before the shock can be amplified by the energetic electrons through the gyro-resonance, we investigate the data of electrons first. Figure 6 displays the phase space density (PSD) of the 3.3-76.4 keV electrons. It is measured by ThE from 1551:03 to 1551:30 UT with an accumulation time of 3 s. The PSD of the 33.5-76.4 keV electrons, which is measured by SST, has been calibrated using the kappa and relativistic kappa-type distribution. It can be seen that before the shock the electron PSD is more isotropic. When the shock arrives at 1551:17 UT (thick frame), the electron PSD shows a peak at 90° pitch angle. This perpendicular distribution is

prominent for the >15 keV electrons but not very clear for the <15 keV electrons. After 1551:21 UT, the perpendicular distribution of electrons is also not clear. The electron PSDs at 1551:06 and 1551:15 UT will be analyzed in detail. One is measured at the quiet time (1551:06 UT), while the other is during the compression of magnetosphere (1551:15 UT).

Since the choruses are observed by ThE near the geomagnetic equator (Figure 4e-4f), it is reasonable to assume that these choruses propagate along the magnetic field line [e.g., *Hayakawa et al.*, 1984; *Santolík* and *Gurnett*, 2003]. The relativistic cyclotron resonance condition for the parallel and anti-parallel mode chorus can be expressed as [e.g., *Brice*, 1964; *Omura and Summers*, 2006; *Rycroft,* 1976]

$$\omega - k_{\parallel} v_{\parallel} = \omega_{ce} \left(1 - \frac{v_{\parallel}^2 + v_{\perp}^2}{c^2} \right)^{1/2} \qquad (4)$$

where ω represents the angular frequency of chorus, while $k_{//}$ the parallel component of the wave vector of chorus. The quantities $v_{//}$ and $v_{\perp}$ denote, respectively, the parallel and perpendicular velocity of the resonant electrons. The right side of the equation expresses the angular gyro-frequency of the relativistic electron, which is smaller than the general gyro-frequency ω_{ce} especially when the velocity of electrons is comparable to the speed of light c. Among the quantities in equation (4), ω, ω_{ce} and $k_{//}$ can be obtained from the observations of ThE. The relation between other two parameters, $v_{//}$ and $v_{\perp}$, thus can be determined.

Figure 7a shows the pitch angle of resonant electrons (dashed and dotted black curves) together with the PSD of the 3.3-76.4 keV electrons at 1551:06 UT (before

shock). This PSD distribution is same as that shown in the second panel of Figure 6. The lower-band chorus with frequency from 0.1 f_{ce} to 0.45 f_{ce} is considered at this time. Their resonances with energetic electrons are expressed by the dashed (0.1 f_{ce}) and dotted (0.45 f_{ce}) black curves. The left resonance curve is produced by the parallel mode chorus, while the right resonance curve is produced by the anti-parallel mode chorus. Only the electrons between the dashed and dotted black line can interact with the lower-band chorus at 1551:06 UT. We notice that the chorus with frequency of 0.45 f_{ce} can interact with the very-low-energy electrons, while the chorus with frequency of 0.1 f_{ce} cannot interact with the <10 keV electrons. The thick black lines represent the diffusion curves of electrons produced by the parallel (left) and anti-parallel (right) lower-band chorus [e.g., *Kennel and Petschek*, 1966]. They can be described by the equation [*Summers at el.*, 1998]

$$\left(1-v_{ph}v_{//}\right)v_{\perp}dv_{\perp}+\left(v_{//}-v_{ph}+v_{ph}v_{\perp}^{2}\right)dv_{//}=0 \quad (5)$$

where $v_{//}$ and $v_{\perp}$ are the parallel and perpendicular velocity of the electrons along the diffusion curves (thick black lines in Figure 7a). v_{ph} is the phase velocity of the wideband chorus; it is a function of wave frequency that ranges from 0.1 f_{ce} to 0.45 f_{ce} in Figure 7a. All velocities in equation (5) have been normalized by the speed of light c. Since v_{ph} is not a constant, the integration of equation (5) is nontrivial. On the diffusion curves in Figure 7a, the arrows indicate the diffusion direction of electrons.

To compare with the previous studies [e.g., *Meredith et al.*, 2002], we also plot the diffusion curves produced by the single-frequency wave. In Figure 7a, the left solid white line indicates the diffusion curve produced by the parallel mode chorus with frequency of 0.45 f_{ce}, while the right solid white line is the diffusion curve produced by the anti-

parallel mode chorus with frequency of 0.45 f_{ce}. They are described by the formula [e.g., *Walker* 1993; *Summers at el.*, 1998].

$$\left(v_{//} - v_{ph}\right)^2 + v_{\perp}^2 = (v_{ph} - v_{res})^2 + (v_e^2 - v_{res}^2) \quad (6)$$

where $v_{//}$ and $v_{\perp}$ are the parallel and perpendicular velocity of the electrons along the diffusion curve (solid white lines in Figure 7a). v_{ph} is the phase velocity of this single-frequency wave; it is positive for the parallel propagating mode but negative for the anti-parallel propagating mode (see the two green dots in Figure 7a). v_{res} represents the parallel velocity of resonant electrons; it has the same meaning as the quantity "$v_{//}$" in equation (4). For the parallel propagating chorus, v_{res} is negative; while for the anti-parallel propagating chorus, v_{res} is positive. v_{res} is determined by both the relativistic velocity of electrons and the frequency of chorus. v_e represents the relativistic velocity of resonant electrons. All velocities in formula (6) have been normalized by the speed of light c.

To avoid the confusion, it is necessary to state that the quantities $v_{//}$ and $v_{\perp}$ in equation (4) are used to describe the resonance curves, while the quantities $v_{//}$ and $v_{\perp}$ in equation (5) and (6) are used to describe the diffusion curves. The diffusion curve produced by wideband chorus can be decomposed into many elements. Every element is produced by the single wave with different frequency [*Summers at el.*, 1998]. The thick black curves in Figure 7a are actually obtained with this method, but not equation (5).

We can see that, in Figure 7a, the diffusion curves created by the wideband chorus and single-frequency (0.45 f_{ce}) wave are almost the same in this case. This situation,

however, cannot be always true especially when the pitch angle diffusion (Δα) is strong. In fact, the single-frequency chorus can only scatter the electrons near the resonance point. In the region far away from the resonance point, the cyclotron resonance condition (equation 4) is not satisfied for single-frequency wave. In this way, the wideband chorus should be taken into account during the analysis of wave-particle interaction.

Since ThE is located in the quiet plasmatrough at 1551:06 UT, the electron PSD shown in Figure 7a is almost isotropic. We examine the resonance between the lower-band chorus and the higher-energy electrons. The 60.1 keV electrons, which are measured by SST, are investigated in detail. Their PSDs are indicated by the white dashed half-circle in Figure 7a. When the 60.1 keV electrons interact with the wideband chorus, they can be scattered along the diffusion curve from high-density region to low-density region. Figure 7b and 7c show the electron PSD and energy loss along the parallel diffusion curve (left black thick curve in Figure 7a). The arrows indicate the diffusion direction.

Figure 8 is plotted in the similar format as Figure 7 but for investigating the resonance process at 1551:15 UT (after shock). The interaction between the 60.1 keV electrons and the 0.1 - 0.45 f_{ce} wideband chorus are considered at this time. Due to the compression of magnetosphere, the equatorial gyro-frequency f_{ce} at 1551:15 UT is slightly larger than that at 1551:06 UT. We see that, in Figure 8a, the PSD of higher-energy electrons shows a peak near the 90° pith angle, just same as the PSD shown in the fifth panel of Figure 6. These electrons are unstable and can be scattered along the diffusion curve from resonance point to low-density region. Figure 8b and 8c show the

electron PSD and energy loss along the parallel diffusion curve (left black thick line in Figure 8a).

The parameters for the electron diffusion in Figure 7b-7c and Figure 8b-8c are summarized in Table 1. The left column corresponds to the diffusion before shock (Figure 7), while the right column corresponds to the diffusion after shock (Figure 8). As can be seen, the Pitch angle diffusion ($\Delta\alpha$) and Energy loss (ΔE) are quite similar for the process before and after the shock. The PSD gradient ($\Delta N/\Delta\alpha$) after the shock, however, is about 10 times larger than that before the shock. This means the electron diffusion after the shock is more effective than that before the shock. During the diffusion process, the electrons lose energies. This energy can them be transferred to amplify the chorus. Since the electron diffusion after the shock is more effective, the chorus amplification after the shock should be significant. This linear diffusion process can qualitatively explain the observation in Figure 4 and 5.

We also investigate the gyro-resonance between the lower-band chorus and the low energy electrons that are measured by ESA. The data of these low energy electrons are basically reliable so need not further calibration. The 24.5 keV electrons are studied as an example. Figure 9 shows the resonance and diffusion curves of the 24.5 keV electrons before the shock at 1551:06 UT, while Figure 10 shows them after the shock at 1551:15 UT. Figure 9 and 10 are plotted in the similar format as Figure 7. Since the pitch angle diffusion is strong for these low energy electrons, we can see that in Figure 9 and 10 the diffusion curve produced by the wideband chorus is a little different from that produced by the single-frequency (0.45 f_{ce}) wave. This difference is clearer near the black dashed lines. The PSD and energy loss of the 24.5 keV electrons along the parallel diffusion

curve are shown in Figure 9b-9c and Figure 10b-10c. The corresponding parameters are listed in Table 2, where the left column is for the diffusion before shock (Figure 9), and the right column is for the diffusion after shock (Figure 10). Seen from Table 2, the Pitch angle diffusion ($\Delta\alpha$) after the shock is slightly stronger than that before the shock; the Energy loss (ΔE) before and after the shock is almost the same; the PSD gradient ($\Delta N/\Delta\alpha$) after the shock is about 2 times as larger as that before the shock. Similar as the 60.1 keV electrons, the diffusion of the 24.5 keV electrons after the shock is more effective than that before the shock. The chorus after shock thus will gain more energy and should be more intense.

The comparison between the 60.1 keV and 24.5 keV electrons can be used to investigate whether the higher-energy electrons or the lower-energy electrons contribute more to the diffusion and the chorus intensification. At 1551:15 UT, the PSD gradient of the 24.5 keV electrons ($\Delta N/\Delta\alpha \approx 2.19\times10^{-20}$ $s^3/m^6/deg$) is about 3 times as lager as that of the 60.1 keV electrons ($\Delta N/\Delta\alpha \approx 6.59\times10^{-21}$ $s^3/m^6/deg$), while the energy losses for the 24.5 keV ($\Delta E \approx 2.7$ keV) and 60.1 keV ($\Delta E \approx 3.0$ keV) electrons are very similar. At 1551:06 UT, the PSD gradient of the 24.5 keV electrons is even 15 times lager than that of the 60.1 keV electrons, and the energy losses are similar. This indicates that, in this event, the lower-energy electrons contribute more to the chorus intensification.

In Figure 7-10, the resonance curves (dashed and dotted black lines) are calculated using the relativistic cyclotron resonance condition (equation 4). However, they look like vertical straight lines. This means the relativistic effect is not important for the <80 keV electrons. In this way, we can evaluate the nonrelativistic linear growth rate with the formula [*Kennel and Petschek*, 1966; *Hikishima et al.*, 2009; *Li et al.*, 2011a].

$$\omega_i = \pi\omega_{ce}\left(1-\frac{\omega}{\omega_{ce}}\right)^2 \eta\left(V_{R0}\right)\left[A\left(V_{R0}\right)-A_c\right] \quad (7)$$

where ω_{ce} and V_{R0} represent the gyro-frequency and parallel velocity of the resonant electrons. $\eta\left(V_{R0}\right)$, $A\left(V_{R0}\right)$ and A_c represent, respectively, the density, temperature anisotropy of resonant electrons, and the critical temperature anisotropy. They are defined as

$$\eta\left(V_{R0}\right) = 2\pi\frac{\omega_{ce}-\omega}{k}\int_0^\infty v_\perp F dv_\perp\Big|_{v_{//}=V_{R0}} \quad (8)$$

$$A\left(V_{R0}\right) = \frac{\int_0^\infty\left(v_{//}\frac{\partial F}{\partial v_\perp}-v_\perp\frac{\partial F}{\partial v_{//}}\right)\frac{v_\perp^2}{v_{//}}dv_\perp}{2\int_0^\infty v_\perp F dv_\perp}\Big|_{v_{//}=V_{R0}} \quad (9)$$

$$A_c = \frac{1}{\omega_{ce}/\omega-1} \quad (10)$$

Figure 11 shows the linear growth rate of chorus at 1515:06 UT (a) and 1515:15 UT (b). As can be seen, the positive growth rates are between 0.05 f_{ce} and 0.3 f_{ce}, roughly consistent with the frequency range of the lower-band chorus. Before the shock (Figure 11a), the maximum growth rate is $\omega_i/\omega_{ce}\approx 0.04$ and appears at f≈200 Hz. After the shock (Figure 11b), the maximum growth rate is $\omega_i/\omega_{ce}\approx 0.06$ and appears at f≈300 Hz. The maximum growth rate after shock is about 50% larger than that before the shock. Thus it may be responsible for the strong intensity of chorus observed after the shock. Since the plasma density decreases at ~1551:13 UT (see dotted lines in Figure 5), the maximum growth rate shift from at f≈200 Hz (before shcok) to at f≈300 Hz (after shcok).

This is consistent with the numerical results of *Hikishima et al.* [2009, see figure 2a there]. The largest damp rate is obtained near 0.5 f_{ce}, consistent with the gap of chorus (see Figure 5). For the upper-band chorus (0.5 - 0.7 f_{ce}), the amplitude is not large (Figure 5). This agrees with the small damp rates in Figure 11a and 11b. Here we should point out that the linear grow rates of the 0.3 - 1.0 f_{ce} chorus in Figure 11 may be not very accurate because the low energy (<3 keV) electrons are not taken into account during the calculation (see the white space in Figure 7a-10a).

5. Energy source

In this section, we investigate the free energy for the chorus intensification. The local betatron acceleration and radial diffusion are considered respectively.

5.1 Local betatron acceleration

Figure 12 schematically illustrates the process of local betatron acceleration. Before the shock at 1551:06-09 UT, ThE observes a regular magnetic field; while after the shock at 1551:15-18 UT, ThE observes a shock-induced enhancement of magnetic field. The compression of magnetosphere lasts for ~20 s (Figure 4f). This is much shorter than the drift period (~2 hour) of the local 40 keV electrons, but much longer than the cyclotron period (~1.0×10^{-3} s) of the 40 keV electrons. Therefore, during the compression of magnetosphere, the first adiabatic invariant $\mu = E_{\perp} / B$ should be conserved. This can lead to the betatron acceleration of electrons and then the increase of pitch angle, as indicated by the thick frame of Figure 6.

We examine quantitatively whether the local betatron acceleration can be responsible for the free energy. Figure 13a and 13b show, respectively, the electron PSDs

at 1551:06 UT (a) and 1551:15 UT (b). We can see that, at 1551:06 UT, the electron PSD is nearly isotropic although small peaks are observed around α≈90° for the 60-76 keV electrons. At 1551:15 UT, the electrons clearly peak at α≈90° (solid lines) especially for the >15 keV electrons. Since the drift period of these electrons is very long (~2 hour), it is reasonable to assume that the < 80 keV electrons observed at 1551:06 UT and 1551:15 UT are the same population. In this way, we can treat the electrons at 1551:06 UT as the source, and then reproduce the electrons at 1551:15 UT with the betatron acceleration model $E_{1\perp} = (B_1 / B_0) \cdot E_{0\perp} = F_b \cdot E_{0\perp}$, where $E_{0\perp}$ and $E_{1\perp}$ represent, respectively, the perpendicular energy of electrons before and after the shock. The parallel energy of electrons does not change during the betatron acceleration process. Before the shock at 1551:06 UT, the magnetic field strength is B_0≈53 nT, while after the shock at 1551:15 UT, the magnetic field strength is B_1≈55 nT. The factor of betatron acceleration is thus determined to be F_b≈1.04 in this case. We plot the modeling results in Figure 13b as dashed lines. As can be seen, the modeling results are roughly consistent with the observations of ThE. The observed PSD is slightly larger than the modeling results, indicating that the local betatron acceleration can contribute partly to the free energy. For the low energy (<10 keV) electrons, the betatron acceleration is not effective. This is a normally expected situation as illustrated in the previous studies [e.g., *Birn et al.,* 2004; *Fu et al.,* 2011b].

5.2 Radial diffusion

The inward radial diffusion, which yields to the violation of the third adiabatic invirant, may also lead to the perpendicular acceleration of electrons. Radial diffusion is driven by the drift-resonance between the electrons and the ULF waves in the range of

Pc4 (45-150 s) and Pc5 (150-600 s) pulsations [e.g., *Throne*, 2010; *Su et al.*, 2011]. Figure 14 investigates the possiblity of radial diffusion as a meachnism producing the free energy in this event. From top to bottom, the spectrogram of magnetic filed (a) and electric field (b), the dEFs of the 20-25 keV electrons (c) are shown in the period range of 8-1024 s. The coherences between magnetic field and dEFs are shown in Figure 14d, while the coherences between electric field and dEFs are shown in Figure 14e. The two dashed lines in Figure 14a-14e indicate the period of 45 s and 600 s. They cover the range of Pc4 and Pc5 pulsations. When the interplanetary shock compresses the magnetosphere at 1551:15 UT (vertical arrow), the good coherences between ULF waves and dEFs are observed (Figure 14d-14e). This means the ULF waves can interact with the energetic electrons, and then lead to the radial diffusion. The ULF waves in the range of Pc4 and Pc5 pulsations, thus, may supply free energies for the chorus intensification. This is consistent with the recent study of *Li et al.* [2011a].

In Figure 14f, the AE index is plotted. We find a small substorm event at ~1556 UT. During this substorm, energetic electrons may inject from the magnetotail to the inner magnetosphere. However, it should be pointed out that these injected electrons cannot contribute to the chorus intensification because they are observed about 5 minutes later. In fact, if the energetic electrons injected from magnetotail contribute to the chorus intensification, ThA should observe the intensification earlier than ThD (see Figure 2d). However, this is not the case (see Figure 4).

6. Summary and conclusions

In this paper, we studied a chorus intensification event on 3 September 2009. The event is observed by THEMIS in the dayside plasmatrough region when an interplanetary shock compresses the magnetosphere. We analyzed in detail the gyro-resonance condition between chorus and energetic electrons. We find that the lower-band chorus can scatter the electrons from resonance points to low density region. During the diffusion process, the electron energy can be partly lost and then transferred to amplify the chorus. Since the temperature anisotropy of electrons after the shock is much larger than that before the shock, the diffusion processes and chorus intensification after the shock are more prominent. We calculated the linear growth rates and found that the maximum growth rate after the shock is about 50% greater than that before the shock. The lower-energy (15 - 25 keV) electrons contribute more to the chorus intensification due to the larger density gradient along the diffusion curve. The < 10 keV electrons are almost isotropic during the compression of magnetosphere. Their contribution to the chorus intensification thus is not important. The energy source for the chorus intensification was also investigated. Both local betatron acceleration and radial diffusion can supply free energies for the chorus intensification. The substorm-injected electrons from magnetotail are not expected to contribute to free energies in this event because they appear ~5 minutes after the chorus intensification.

We have also investigated another chorus intensification event on 19 November 2007 [*Fu et al.*, 2011c]. We find a similar situation in this case that the chorus is amplified significantly when the interplanetary shock hits the Earth's magnetosphere. Both radial diffusion and betatron acceleration, which results from the shock-induced compression of magnetic field, can provide free energies for the chorus intensification.

This means the shock-associated intensification of chorus may be a common phenomenon, and the local betatron acceleration of electrons should be emphasized in the future as the energy source.

7. **Discussions**

Betatron acceleration requires the conservation of the first invariant, while radial diffusion requires the conservation of the first and second adiabatic invariants but the violation of the third adiabatic invariant. During the gyro-resonance and diffusion process, all three adiabatic invariants are violated. Therefore, in the different stage of chorus intensification, different adiabatic invariants should be taken into account.

7.1 Linear and nonlinear growth rate

Chorus intensification involves both the linear and nonlinear processes [e.g., *Santolik*, 2008; *Hikishima et al.,* 2009; *Macúšová et al.,* 2010]. The linear process plays a dominant role in the early stage, while the nonlinear process is important in the later stage and will lead to the saturation of waves [e.g., *Omura et al.*, 2008; *Hikishima et al.,* 2009]. *Hikishima et al.* [2009] pointed out that the linear growth rate of chorus (see formula (6) there) is determined by f_{pe}/f_{ce} (ratio of plasma frequency to gyro-frequency), A (temperature anisotropy) and N_h/N_c (ratio of hot electron density to cold electron density). The large value of f_{pe}/f_{ce}, A and N_h/N_c will give rise to a large linear growth rate during the chorus generation process (see Figure 3 there). The nonlinear growth rate of chorus is also determined by f_{pe}/f_{ce} [*Omura et al.,* 2009, see formula (22) there]. Large value of f_{pe}/f_{ce}, however, will give rise to the small nonlinear growth rate (see Figure 1 there). *Omura et al.* [2009] pointed out that the linear growth rate is maximum at the magnetic

equator; the nonlinear growth rate becomes important when the chorus propagates away from the equatorial plane. This nonlinear growth process is attributed to the increasing gradients of the static magnetic field and electron density along the magnetic field line.

In the present case, the chorus intensification was observed by ThE near the equatorial plane (MLAT≈-11°) and in the dayside plasmatrough region (L≈9, MLT≈12). In this region, the gradients of static magnetic field and electron density along the magnetic field line are very small especially at MLAT<20° [e.g., *Huang et al.*, 2004; *Fu et al.*, 2010a; 2010b]. So the linear growth rate should be much larger than the nonlinear growth rate. We also examine the plasma frequency and electron gyro-frequency in this event. At 1551:15 UT (after shock), the plasma frequency is f_{pe}≈ 21.7 kHz, and the electron gyro-frequency is f_{ce}≈1.5 kHz. The large ratio of f_{pe}/f_{ce}≈14 will give rise to a large linear growth rate, but a small nonlinear growth rate. The parameters A and N_h/N_c are considerable large after the shock due to the betatron acceleration and radial diffusion. This will also lead to the large linear growth rate. According to all these criteria, the linear diffusion process assumed in the present study is reasonable. The investigation of the nonlinear process is beyond the scope of our study.

7.2 Wave-particle interaction as energy source?

The chorus before the shock is possible to accelerate electrons and simultaneously enhance the anisotropy of electron distribution. This acceleration and anisotropization process may be effective for the > 200 keV electrons. For the < 80 keV electrons, the distribution function is already slightly anisotropic before the shock (see the second panel of Figure 6). Hence the chorus is difficult to accelerate these electrons. On the contrary,

the < 80 keV electrons may transfer some energy to this seed chorus (see Figure 7c, Figure 9c). There is an "anchor point" at a few 100 keV above which chorus tends to preferentially accelerate/anisotropize electrons, and below which chorus tends to dissipate/isotropize electrons [e.g., *Summers et al.,* 2002; *Bortnik and Thorne* 2007; *Fu et al.*, 2011a]. The low-energy (<100 keV) electrons can transfer their energy to the high-energy (> 200 keV) electrons trough the chorus. This dual role of chorus was suggested as a mechanism responsible for the origin of the 1 MeV electrons in the radiation belt [e.g., *Horne et al.*, 2005b]. Therefore, the acceleration/anisotropization of electrons induced by the chorus, and the diffusion/isotropization of electrons induced by the chorus, are corresponding to different energy channels. The acceleration of electrons will not supply free energies for the chorus intensification in this event especially when the frequency of chorus is only slightly changed before and after the shock (see Figure 5). To avoid the confusion, here we must clarify that the word "anisotropization" means the electrons moves from ~0° or ~180° pitch angle to ~90° pitch angle. It is a description of the PSD for all electrons but not for the resonant electrons. In fact, for the resonant electrons, all diffusion processes are the isotropization processes because the resonant electrons can only diffuse from high-density region to low-density region.

7.3 Future work

The lower-energy (15-25 keV) electrons contribute more to the chorus intensification in this event. This situation, however, may vary in other events. Actually, whether the lower-energy or higher-energy electrons contribute more to the chorus amplification is determined totally by the distribution of phase space density. We use AE index to monitor the substorm-injected electron from magnetotail. This may be not

accurate and should be improved in the future with more reliable observations. Even through the plasma density derived from the spacecraft potential can be affected by the temperature variations, it is more reliable than the ion/electron density measured by ESA directly in most cases [e.g., *McFadden et al.,* 2008b; *Fu et al.*, 2011a]. The comparison between betatron acceleration and radial diffusion should also be given in the future to distinguish which one contributes more to the free energy of electrons.

Acknowledgements.

This work was supported by NSFC grant 40931054, 973 program 2011CB811404. We greatly acknowledge the THEMIS investigators for the use of the data and the analysis software. Specifically, we thank C. W. Carlson and J. P. McFadden for the use of ESA data, D. Larson and R. P. Lin for the use of SST data, K. H. Glassmeier, U. Auster, and W. Baumjohann for the use of FGM data, J. W. Bonnell for the use of EFI data, and A. Roux and O. LeContel for the use of SCM data. The solar wind and IMF data were obtained from Omni on the NASA CDAWeb (http://cdaweb.gsfc.nasa.gov).

Masaki Fujimoto thanks the reviewers for their assistance in evaluating this paper.

References

Angelopoulos, V. (2008), The THEMIS Mission, *Space Sci. Rev.*, 141, 5–34, doi:10.1007/s11214-008-9336-1.

Auster, H. U., et al. (2008), The THEMIS Fluxgate Magnetometer, *Space Sci. Rev.*, 141, 235–264, doi:10.1007/s11214-008-9365-9

Baker, D. N., S. G. Kanekal, X. Li, P. Monk, J. Goldstein, and J. L. Burch (2004), An extreme distortion of the Van Allen belt arising from the 'Hallowe'en' solar storm in 2003, *Nature*, 432, 878-881.

Bonnell, J. W., F. S. Mozer, G. T. Delory, A. J. Hull, R. E. Ergun, C. M. Cully, V. Angelopoulos, and P. R. Harvey (2008), The Electric Field Instrument (EFI) for THEMIS, *Space Sci. Rev.*, 141, 303-341, doi:10.1007/s11214-008-9469-2

Bortnik, J., and R.M. Thorne (2007), The dual role of ELF/VLF chorus waves in the acceleration and precipitation of radiation belt electrons, *J. Atmos. & Solar-Terr. Phys.*, 69, 378–386.

Bortnik, J., R. M. Thorne, and N. P. Meredith (2008), The unexpected origin of plasmaspheric hiss from discrete chorus emissions, *Nature*, 452, 62-66.

Bortnik, J., W. Li, R. M. Thorne, V. Angelopoulos, C. Cully, J. Bonnell, O. Le Contel, and A. Roux (2009), An Observation Linking the Origin of Plasmaspheric Hiss to Discrete Chorus Emissions, *Science*, 324, 775-778.

Birn, J., M. F. Thomsen, and M. Hesse (2004), Electron acceleration in the dynamic magnetotail: Test particle orbits in three□dimensional magnetohydrodynamic simulation fields, *Phys. Plasmas*, 11, 1825–1833, doi:10.1063/1.1704641.

Brice, N. (1964), Fundamentals of Very Low Frequency Emission Generation Mechanisms, *J. Geophys. Res.*, 69(21), 4515-4522.

Bunch, N. L., M. Spasojevic, and Y. Y. Shprits (2011), On the latitudinal extent of chorus emissions as observed by the Polar Plasma Wave Instrument, *J. Geophys. Res.*, 116, A04204, doi:10.1029/2010JA016181

Burtis, W. J., and R. A. Helliwell (1969), Banded Chorus—A New Type of VLF Radiation Observed in the Magnetosphere by OGO 1 and OGO 3, *J. Geophys. Res.*, 74(11), 3002–3010, doi:10.1029/JA074i011p03002.

Burton, R. K., and R. E. Holzer (1974), The Origin and Propagation of Chorus in the Outer Magnetosphere, *J. Geophys. Res.*, 79(7), 1014–1023, doi:10.1029/JA079i007p01014.

Cairns, I. H., D. H. Fairfield, R. R. Anderson, V. E. H. Carlton, K. I. Paularena, and A. J. Lazarus (1995), Unusual Locations of Earth's Bow Shock on September 24 - 25, 1987: Mach Number Effects, *J. Geophys. Res.*, 100(A1), 47-62, doi:10.1029/94JA01978.

Cao, J. B., J. Y. Yang, C. X. Yan, and L. Y. Li (2007), The observations of high energy electrons and associated waves by DSP satellites during substorm, *Nucl. Phys. B*, *166*, 56–61, suppl., doi:10.1016/j.nuclphysbps.2006.12.066

Cully, C. M., V. Angelopoulos, U. Auster, J. Bonnell, and O. Le Contel (2011), Observational evidence of the generation mechanism for rising-tone chorus, *Geophys. Res. Lett.*, *38*, L01106, doi:10.1029/2010GL045793.

Farris, M. H., S. M. Petrinec, and C. T. Russell (1991), The thickness of the magnetosheath: Constraints on the polytropic index, *Geophys. Res. Lett.*, 18(10), 1821–1824, doi:10.1029/91GL02090.

Fu, H. S., J. Tu, P. Song, J. B. Cao, B. W. Reinisch, and B. Yang (2010a), The nightside-to-dayside evolution of the inner magnetosphere: Imager for Magnetopause-to-Aurora Global Exploration Radio Plasma Imager observations, *J. Geophys. Res.*, 115, A04213, doi:10.1029/2009JA014668.

Fu, H. S., J. Tu, J. B. Cao, P. Song, B. W. Reinisch, D. L. Gallagher, and B. Yang (2010b), IMAGE and DMSP observations of a density trough inside the plasmasphere, *J. Geophys. Res.*, 115, A07227, doi:10.1029/2009JA015104.

Fu, H. S., J. B. Cao, B. Yang, and H. Y. Lu (2011a), Electron loss and acceleration during storm time: The contribution of wave-particle interaction, radial diffusion, and transport processes, *J. Geophys. Res.*, *116*, A10210, doi:10.1029/2011JA016672.

Fu, H. S., Y. V. Khotyaintsev, M. André, and A. Vaivads (2011b), Fermi and betatron acceleration of suprathermal electrons behind dipolarization fronts, *Geophys. Res. Lett.*, *38*, L16104, doi:10.1029/2011GL048528.

Fu, H., J. Cao, F. S. Mozer, and B. Yang (2011c), Chorus variation during the compression of magnetosphere, XXXth URSI General Assembly and Scientific Symposium 2011 (URSI GASS 2011), 13-20 August 2011, Istanbul, Turkey.

Gail, W. B., U. S. Inan, R. A. Helliwell, D. L. Carpenter, S. Krishnaswamy, T. J. Rosenberg, and L. J. Lanzerotti (1990), Characteristics of wave-particle interactions during sudden commencements 1. Ground-based observations, *J. Geophys. Res.*, *95*(A1), 119–137.

Gail, W. B., and U. S. Inan (1990), Characteristics of wave-particle interactions during sudden commencements: 2. Spacecraft observations, *J. Geophys. Res.*, *95*(A1), 139–147.

Hayakawa, M., Y. Yamanaka, M. Parrot, and F. Lefeuvre (1984), The Wave Normals of Magnetospheric Chorus Emissions Observed on Board GEOS 2, *J. Geophys. Res.*, 89(A5), 2811–2821, doi:10.1029/JA089iA05p02811.

Helliwell, R. A. (1967), A Theory of Discrete VLF Emissions from the Magnetosphere, *J. Geophys. Res.*, 72(19), 4773–4790, doi:10.1029/JZ072i019p04773.

Hikishima, M., S. Yagitani, Y. Omura, and I. Nagano (2009), Full particle simulation of whistler-mode rising chorus emissions in the magnetosphere, *J. Geophys. Res.*, 114, A01203, doi:10.1029/2008JA013625.

Horne, R. B., et al. (2005a), Wave acceleration of electrons in the Van Allen radiation belts, *Nature*, 437, 227-230.

Horne, R. B., R. M. Thorne, S. A. Glauert, J. M. Albert, N. P. Meredith, and R. R. Anderson (2005b), Timescale for radiation belt electron acceleration by whistler mode chorus waves, *J. Geophys. Res.*, 110, A03225, doi:10.1029/2004JA010811.

Huang, X., B. W. Reinisch, P. Song, J. L. Green, and D. L. Gallagher (2004), Developing an empirical density model of the plasmasphere using IMAGE/RPI observations, *Adv. Space Res.*, 33, 829–833, doi:10.1016/j.asr. 2003.07.007.

Katoh, Y., and Y. Omura (2006), A study of generation mechanism of VLF triggered emission by self-consistent particle code, *J. Geophys. Res.*, 111, A12207, doi:10.1029/2006JA011704.

Katoh, Y., and Y. Omura (2007a), Computer simulation of chorus wave generation in the Earth's inner magnetosphere, *Geophys. Res. Lett.*, 34, L03102, doi:10.1029/2006GL028594.

Katoh, Y., and Y. Omura (2007b), Relativistic particle acceleration in the process of whistler-mode chorus wave generation, *Geophys. Res. Lett.*, 34, L13102, doi:10.1029/2007GL029758.

Kennel, C. F., and H. E. Petschek (1966), Limit on Stably Trapped Particle Fluxes, *J. Geophys. Res.*, 71(1), 1–28, doi:10.1029/JZ071i001p00001.

Kozelov, B. V., A. G. Demekhov, E. E. Titova, V. Y. Trakhtengerts, O. Santolik, E. Macusova, D. A. Gurnett, and J. S. Pickett (2008), Variations in the chorus source location deduced from fluctuations of the ambient magnetic field: Comparison of Cluster data and the backward wave oscillator model, *J. Geophys. Res.*, 113, A06216, doi:10.1029/2007JA012886.

Lauben, D. S., U. S. Inan, T. F. Bell, D. L. Kirchner, G. B. Hospodarsky, and J. S. Pickett (1998), VLF chorus emissions observed by Polar during the January 10, 1997, magnetic cloud, *Geophys. Res. Lett.*, 25(15), 2995–2998, doi:10.1029/98GL01425.

Li, W., R. M. Thorne, N. P. Meredith, R. B. Horne, J. Bortnik, Y. Y. Shprits, and B. Ni (2008), Evaluation of whistler mode chorus amplification during an injection event observed on CRRES, *J. Geophys. Res.*, 113, A09210, doi:10.1029/2008JA013129.

Li, W., R. M. Thorne, V. Angelopoulos, J. W. Bonnell, J. P. McFadden, C. W. Carlson, O. LeContel, A. Roux, K. H. Glassmeier, and H. U. Auster (2009), Evaluation of whistler-mode chorus intensification on the nightside during an injection event observed on the THEMIS spacecraft, *J. Geophys. Res.*, 114, A00C14, doi:10.1029/2008JA013554.

Li, W., et al. (2010), THEMIS analysis of observed equatorial electron distributions responsible for the chorus excitation, *J. Geophys. Res.*, 115, A00F11, doi:10.1029/2009JA014845.

Li, W., R. M. Thorne, J. Bortnik, Y. Nishimura, and V. Angelopoulos (2011a), Modulation of whistler mode chorus waves: 1. Role of compressional Pc4-5 pulsations, *J. Geophys. Res.*, 116, A06205, doi:10.1029/2010JA016312.

Li, W., J. Bortnik, R. M. Thorne, Y. Nishimura, V. Angelopoulos, and L. Chen (2011b), Modulation of whistler mode chorus waves: 2. Role of density variations, *J. Geophys. Res.*, 116, A06206, doi:10.1029/2010JA016313.

Lyons, L. R., D.-Y. Lee, R. M. Thorne, R. B. Horne, and A. J. Smith (2005), Solar wind-magnetosphere coupling leading to relativistic electron energization during high-speed streams, *J. Geophys. Res.*, 110, A11202, doi:10.1029/2005JA011254.

Macúšová, E., et al. (2010), Observations of the relationship between frequency sweep rates of chorus wave packets and plasma density, *J. Geophys. Res.*, 115, A12257, doi:10.1029/2010JA015468.

McFadden, J. P., C.W. Carlson, D. Larson, M. Ludlam, R. Abiad, B. Elliott, P. Turin, M. Marckwordt, and V. Angelopoulos (2008a), The THEMIS ESA Plasma Instrument and In-flight Calibration, *Space Sci. Rev.*, 141, 277–302, doi:10.1007/s11214-008-9440-2

McFadden, J. P., C. W. Carlson, D. Larson, J. Bonnell, F. S. Mozer, V. Angelopoulos, K.-H. Glassmeier, and U. Auster (2008b), Structure of plasmaspheric plumes and their participation in magnetopause reconnection: First results from THEMIS, *Geophys. Res. Lett.*, 35, L17S10, doi:10.1029/2008GL033677.

Meredith, N. P., R. B. Horne, and R. R. Anderson (2001), Substorm dependence of chorus amplitudes: Implications for the acceleration of electrons to relativistic energies, *J. Geophys. Res.*, 106, 13,165–13,178, doi:10.1029/2000JA900156.

Meredith, N. P., R. B. Horne, D. Summers, R. M. Thorne, R. H. A. Iles, D. Heynderickx, and R. R. Anderson, (2002), Evidence for acceleration of outer zone electrons to relativistic energies by whistler mode chorus, *Ann. Geophys.*, 20, 967-979

Meredith, N. P., M. Cain, R. B. Horne, R. M. Thorne, D. Summers, and R. R. Anderson (2003), Evidence for chorus-driven electron acceleration to relativistic energies from a

survey of geomagnetically disturbed periods, *J. Geophys. Res.*, 108(A6), 1248, doi:10.1029/2002JA009764.

Miyoshi, Y., A. Morioka, H. Misawa, T. Obara, T. Nagai, and Y. Kasahara (2003), Rebuilding process of the outer radiation belt during the 3 November 1993 magnetic storm: NOAA and Exos-D observations, *J. Geophys. Res.*, 108(A1), 1004, doi:10.1029/2001JA007542.

Nishimura, Y., et al. (2010), Identifying the driver of pulsating aurora. *Science,* 330, 81-84.

Oliven, M. N., and D. A. Gurnett (1968), Microburst Phenomena, 3, An Association between Microbursts and VLF Chorus, *J. Geophys. Res.*, 73(7), 2355–2362, doi:10.1029/JA073i007p02355.

Omura, Y., D. Nunn, H. Matsumoto, and M. J. Rycroft (1991), A review of observational, theoretical and numerical studies of VLF triggered emissions, *J. Atmos. and Terr. Phys.*, 53, 351– 368.

Omura, Y., and D. Summers (2006), Dynamics of high-energy electrons interacting with whistler mode chorus emissions in the magnetosphere, *J. Geophys. Res.*, 111, A09222, doi:10.1029/2006JA011600.

Omura, Y., Y. Katoh, and D. Summers (2008), Theory and simulation of the generation of whistler-mode chorus, *J. Geophys. Res.*, 113, A04223, doi:10.1029/2007JA012622.

Omura, Y., M. Hikishima, Y. Katoh, D. Summers, and S. Yagitani (2009), Nonlinear mechanisms of lower-band and upper-band VLF chorus emissions in the magnetosphere, *J. Geophys. Res.*, 114, A07217, doi:10.1029/2009JA014206.

Pedersen, A., et al. (2008), Electron density estimations derived from spacecraft potential measurements on Cluster in tenuous plasma regions, *J. Geophys. Res.*, 113, A07S33, doi:10.1029/2007JA012636.

Rodger, C. J., and M. A. Clilverd (2008), Magnetospheric physics: Hiss from the chorus. *Nature*, 452, 41-42.

Roux, A., O. Le Contel, C. Coillot, A. Bouabdellah, B. de la Porte, D. Alison, S. Ruocco, and M. C. Vassal (2008), The Search Coil Magnetometer for THEMIS, *Space Sci. Rev.*, 141, 265-275, doi:10.1007/s11214-008-9455-8

Rycroft, M. (1976), Gyroresonance interactions in the outer plasmasphere, *J. Atmos. and Terr. Phys.*, 38, 1211-1214.

Santolík, O., and D. A. Gurnett (2003), Transverse dimensions of chorus in the source region, *Geophys. Res. Lett.*, 30(2), 1031, doi:10.1029/2002GL016178.

Santolík, O., D. A. Gurnett, J. S. Pickett, M. Parrot, and N. Cornilleau-Wehrlin (2003), Spatio-temporal structure of storm-time chorus, *J. Geophys. Res.*, 108, 1278, doi:10.1029/2002JA009791.

Santolík, O., D. A. Gurnett, and J. S. Pickett (2004), Multipoint investigation of the source region of storm-time chorus, *Ann. Geophys.* 22, 2555-2563.

Santolik, O. (2008), New results of investigations of whistler-mode chorus emissions, *Nonlinear Processes Geophys.*, 15, 621–630.

Sazhin, S. S., and M. Hayakawa (1992), Magnetospheric chorus emissions: A review, *Planet. Space Sci.*, 40, 681– 697.

Shue, J.-H., et al. (1998), Magnetopause location under extreme solar wind conditions, *J. Geophys. Res.*, 103(A8), 17,691–17,700, doi:10.1029/98JA01103.

Su, Z., F. Xiao, H. Zheng, and S. Wang (2011), Radiation belt electron dynamics driven by adiabatic transport, radial diffusion, and wave-particle interactions, *J. Geophys. Res.*, 116, A04205, doi:10.1029/2010JA016228.

Summers, D., R. M. Thorne, and F. Xiao (1998), Relativistic theory of wave-particle resonant diffusion with application to electron acceleration in the magnetosphere, *J. Geophys. Res.*, *103*(A9), 20,487–20,500, doi:10.1029/98JA01740.

Summers, D., C. Ma, N. P. Meredith, R. B. Horne, R. M. Thorne, D. Heynderickx, and R. R. Anderson (2002), Model of the energization of outer-zone electrons by whistler-mode chorus during the October 9, 1990 geomagnetic storm, *Geophys. Res. Lett.*, 29(24), 2174, doi:10.1029/2002GL016039.

Thorne, R. M. (2010), Radiation belt dynamics: The importance of wave-particle interactions, *Geophys. Res. Lett.*, 37, L22107, doi:10.1029/2010GL044990.

Thorne, R. M., B. Ni, X. Tao, R. B. Horne, and N. P. Meredith (2010), Scattering by chorus waves as the dominant cause of diffuse auroral precipitation. *Nature,* 467, 943-946.

Trakhtengerts, V. (1995), Magnetosphere Cyclotron Maser: Backward Wave Oscillator Generation Regime, *J. Geophys. Res.*, 100(A9), 17205-17210.

Tsurutani, B. T., and E. J. Smith (1977), Two Types of Magnetospheric ELF Chorus and Their Substorm Dependences, *J. Geophys. Res.*, 82(32), 5112–5128, doi:10.1029/JA082i032p05112.

Walker, A. D. M. (1993), *Plasma Waves in the Magnetosphere*, Springer-Verlag, New York.

Xiao, F., C. Shen, Y. Wang, H. Zheng, and S. Wang (2008), Energetic electron distributions fitted with a relativistic kappa- type function at geosynchronous orbit, *J. Geophys. Res.*, 113, A05203, doi:10.1029/2007JA012903.

Yang, J. Y., J. B. Cao, C. X. Yan, L. Y. Li, and G. C. Zhou (2007), The acceleration of energetic electrons associated with chorus observed by TC-2, *Nucl. Phys. B*, *166*, 276 – 278, suppl., doi:10.1016/j.nuclphysbps. 2006.12.026.

Yang, J. Y., J. B. Cao, C. X. Yan, L. Y. Li, and Y. D. Ma (2008), The mid- high latitude whistler mode chorus waves observed around substorm onsets, *Sci. China, Ser. E, 51*(10), 1648–1658

Zong, Q.-G., X.-Z. Zhou, Y. F. Wang, X. Li, P. Song, D. N. Baker, T. A. Fritz, P. W. Daly, M. Dunlop, and A. Pedersen (2009), Energetic electron response to ULF waves induced by interplanetary shocks in the outer radiation belt, *J. Geophys. Res.*, 114, A10204, doi:10.1029/2009JA014393.

Tables

Table 1. PSD gradient and energy loss of the 60.1 keV electrons during the diffusion processes before and after the shock.

	1551:06 UT (before shock)	1551:15 UT (after shock)
Pitch angle diffusion	$\Delta\alpha\approx18°$ (94° to 112°)	$\Delta\alpha\approx19°$ (94° to 113°)
PSD decrease	$\Delta N\approx1.205\times10^{-20}$ s^3/m^6 ($10^{-19.305}$ to $10^{-19.426}$ s^3/m^6)	$\Delta N\approx1.253\times10^{-19}$ s^3/m^6 ($10^{-18.60}$ to $10^{-18.90}$ s^3/m^6)
PSD gradient	$\Delta N/\Delta\alpha\approx6.69\times10^{-22}$ $s^3/m^6/deg$	$\Delta N/\Delta\alpha\approx6.59\times10^{-21}$ $s^3/m^6/deg$
Energy loss	$\Delta E\approx2.7$ keV (0.447 c to 0.438 c)	$\Delta E\approx3.0$ keV (0.447 c to 0.437 c)

Table 2. PSD gradient and energy loss of the 24.5 keV electrons during the diffusion processes before and after the shock.

	1551:06 UT (before shock)	1551:15 UT (after shock)
Pitch angle diffusion	$\Delta\alpha\approx32°$ (97° to 129°)	$\Delta\alpha\approx35°$ (97° to 132°)
PSD decrease	$\Delta N\approx3.277\times10^{-19}$ s^3/m^6 ($10^{-17.95}$ to $10^{-18.10}$ s^3/m^6)	$\Delta N\approx7.650\times10^{-19}$ s^3/m^6 ($10^{-17.77}$ to $10^{-18.03}$ s^3/m^6)
PSD gradient	$\Delta N/\Delta\alpha\approx1.02\times10^{-20}$ $s^3/m^6/deg$	$\Delta N/\Delta\alpha\approx2.19\times10^{-20}$ $s^3/m^6/deg$
Energy loss	$\Delta E\approx2.5$ keV (0.299 c to 0.285 c)	$\Delta E\approx2.7$ keV (0.299 c to 0.283 c)

Figure captions

Figure 1. Electron differential energy fluxes (dEFs) before (a, c) and after the calibrations (b, d). The color lines represent the dEFs at pitch angles from α=0 to α=180°. The shadow region indicates the systemic jump between the measurements of ESA (<30 keV) and SST (>30 keV). The black and blue thick lines in Figure 1b and 1d describe, respectively, the relativistic kappa-type distribution [*Xiao et al.*, 2008] and kappa distribution.

Figure 2. The location of ThA (red squares), ThD (black triangles), and ThE (blue dots) at 1550 UT on 3 September 2009. They are shown, respectively, in the *XYgsm* (a), *XZgsm* (b) and *YZgsm* plane (c). Figure 2d also displays the location of bow shock and magnetopause that are calculated with the model [*Farris et al.*, 1991; *Cairns et al.*, 1995; *Shue et al.*, 1998]. The Sun is in the right side of panel (a, b, d), but in the inside of panel (c). All three satellites are close to the subsolar point of the magnetopause. The separations among these three satellites are also quite small.

Figure 3. Solar wind and IMF parameters measured at the Earth's bow shock nose. From top to bottom, the solar wind density (a), solar wind velocity (b), *IMF Bz* (c), and the solar wind dynamic pressure (d) are displayed respectively. The vertical dashed line indicates the arrival of an interplanetary shock, which then compressed the Earth's magnetosphere at 1551 UT.

Figure 4. Spectrogram of VLF waves and the background magnetic field measured by ThA (a-b), ThD (c-d) and ThE(e-f) from 1548 to 1553 UT on 3 September 2009. The wave amplitude is derived from the filter bank (FBK) data; it has been calibrated according to the frequency response characteristics [*Bonnell et al.*, 2008]. The three dashed white lines in panels (a, c, e) represent, from top to bottom, the equatorial gyro-frequency of the electrons f_{ce}, 0.45 f_{ce} and 0.1 f_{ce}. The shadow region in panels (b, d, f) indicate the sudden compression of magnetosphere induced by the interplanetary shcok; it lasts for ~20s. The vertical lines point out the starting time of chorus intensification, and the upward arrows show the largest amplitude of these choruses. Labeled below the abscissa is the orbital information of each satellite including the universe time (UT), *L* value, magnetic local time (MLT), magnetic latitude (MLAT), and the radial distance to the center of the Earth (r) in the unit of R_E.

Figure 5. Spectrogram of VLF waves recorded by ThE in the particle burst mode from 1550:30 to 1552:00 UT on 3 September 2009. The wave amplitude in Figure 5a is measured by axis 2 of the SCM instrument, while the wave amplitude in Figure 5b is measured by axis 3 of SCM. Similar as that in Figure 4, the three white lines represent the equatorial gyro-frequency of the electrons f_{ce}, 0.45 f_{ce} and 0.1 f_{ce}. The blue dotted lines, scaled by the right-side Y-axis, denote the plasma density derived from the spacecraft potential.

Figure 6. Phase space density (PSD) of the 3.3-76.4 keV electrons. It is measured by ThE from 1551:03 to 1551:30 UT with an accumulation time of 3 s. The thick frame indicates a perpendicular distribution during the compression of magnetosphere, which is observed at 1551:15 UT.

Figure 7. (a) PSD of the 3.3-76.4 keV electrons, measured by ThE at 1551:06 UT on 3 September 2009 (before the shock). The dashed half-circle indicates the PSD of the 60.1 keV electrons that are set an example to investigate the chorus-electron interaction. The wideband chorus from 0.1 f_{ce} to 0.45 f_{ce} is considered as the wave interacting with the energetic-electrons at this time. Their resonance curves are expressed by the dashed (0.1 f_{ce}) and dotted (0.45 f_{ce}) black lines, respectively. Left resonance curve is created by the parallel mode chorus, while right resonance curve is created by the anti-parallel mode chorus. Only the electrons between the dashed and dotted lines can interact with the wideband chorus. The black thick lines represent the diffusion curve created by the parallel (left) and anti-parallel (right) wideband chorus. The diffusion directions of the 60.1 keV electrons are shown by the black arrows. The white solid lines denote the diffusion curves created by the single-frequency (0.45 f_{ce}) wave. When the pitch angle diffusion ($\Delta\alpha$) is strong, the diffusion curves created by the single-frequency wave and wideband chorus are quite different. The electron velocities in Figure 7a have been normalized by the speed of light c; their corresponding energies measured by ESA and SST are listed on the right side. (b) Electron PSD along the left diffusion curve in Figure 7a. (c) Electron energy along the left diffusion curve in Figure 7a. The arrows in Figure

7b and 7c also indicate the diffusion direction of the electron, i.e. from high-density region to low-density region.

Figure 8. Similar format as Figure 7 but for investigating the resonance process between the 60.1 keV electrons and the 0.1 - 0.45 f_{ce} wideband chorus at 1551:15 UT (after the shock). The equatorial gyro-frequency f_{ce} at 1551:15 UT (after shock) is slightly larger than that at 1551:06 UT (before shock) due to the compression of magnetosphere.

Figure 9. Similar format as Figure 7 but for investigating the resonance process between the 24.5 keV electrons and the 0.1 - 0.45 f_{ce} wideband chorus at 1551:06 UT (before the shock).

Figure 10. Similar format as Figure 7 but for investigating the resonance process between the 24.5 keV electrons and the 0.1 - 0.45 f_{ce} wideband chorus at 1551:15 UT (after the shock).

Figure 11. Nonrelativistic linear growth rate of chorus before (a) and after the shock (b). The growth rate and frequency of chorus has been normalized by the equatorial gyro-frequency of electrons.

Figure 12. A cartoon illustrating the anisotropization process of the electrons in response to the interplanetary shock. Top panel shows the quite-time magnetosphere, while bottom panel shows the compression of magnetosphere by the shock. After the shock, the magnetic field is enhanced and the gyro-radius of electrons becomes smaller.

Figure 13. Evolution of the electron PSD from 1551:06 UT (before the shock) to 1551:15 UT (after the shock). The solid lines represent the observations of ThE, while the dashed lines represent the results calculated from the model of betatron acceleration.

Figure 14. Wavelet power spectrogram of the magnetic field (a), electric field (b), and the differential-energy-fluxes (dEFs) of the 20-25 keV electrons (c) during the period 15:30 – 16:30 UT on 3 September 2009. Panel (d) shows the coherence analysis between the magnetic field and the dEFs, while panel (e) shows the coherence analysis between the electric field and the dEFs. The upper and low dashed lines in panel (a-e) indicate, respectively, the period of 45 s and 600 s. They cover the range of Pc4 and Pc5 pulsations. Panel (f) shows the AE index recorded on the ground. The vertical arrow in Figure 14 indicates the arrival of an interplanetary shock at 15:51 UT.

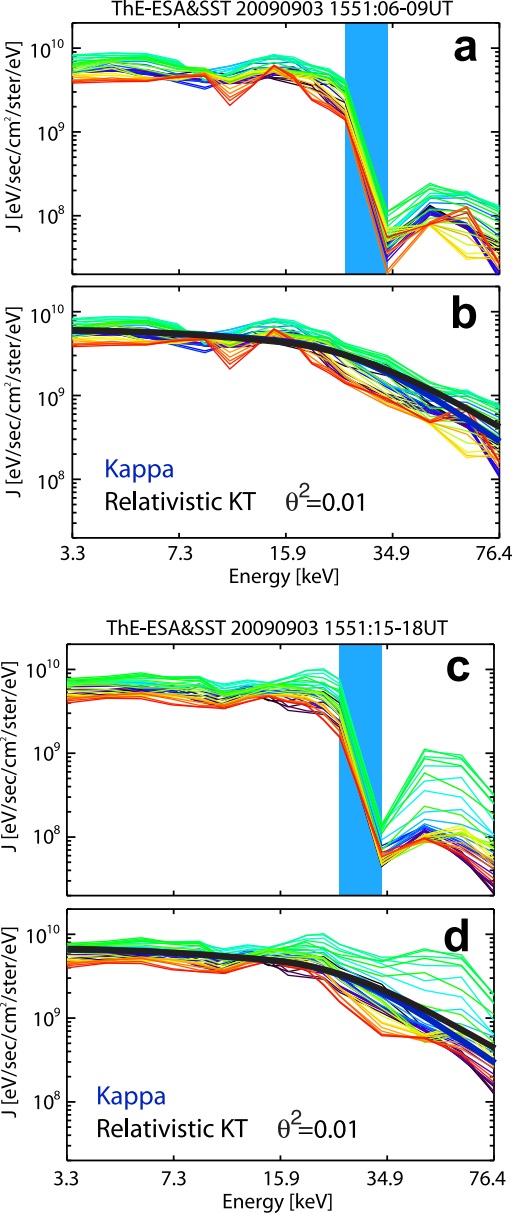
ThE-ESA&SST 20090903 1551:06-09UT
a
b
J [eV/sec/cm²/ster/eV]
10^{10}
10^{9}
10^{8}
Kappa
Relativistic KT θ^2=0.01
3.3
7.3
15.9
34.9
76.4
Energy [keV]
ThE-ESA&SST 20090903 1551:15-18UT
c
d

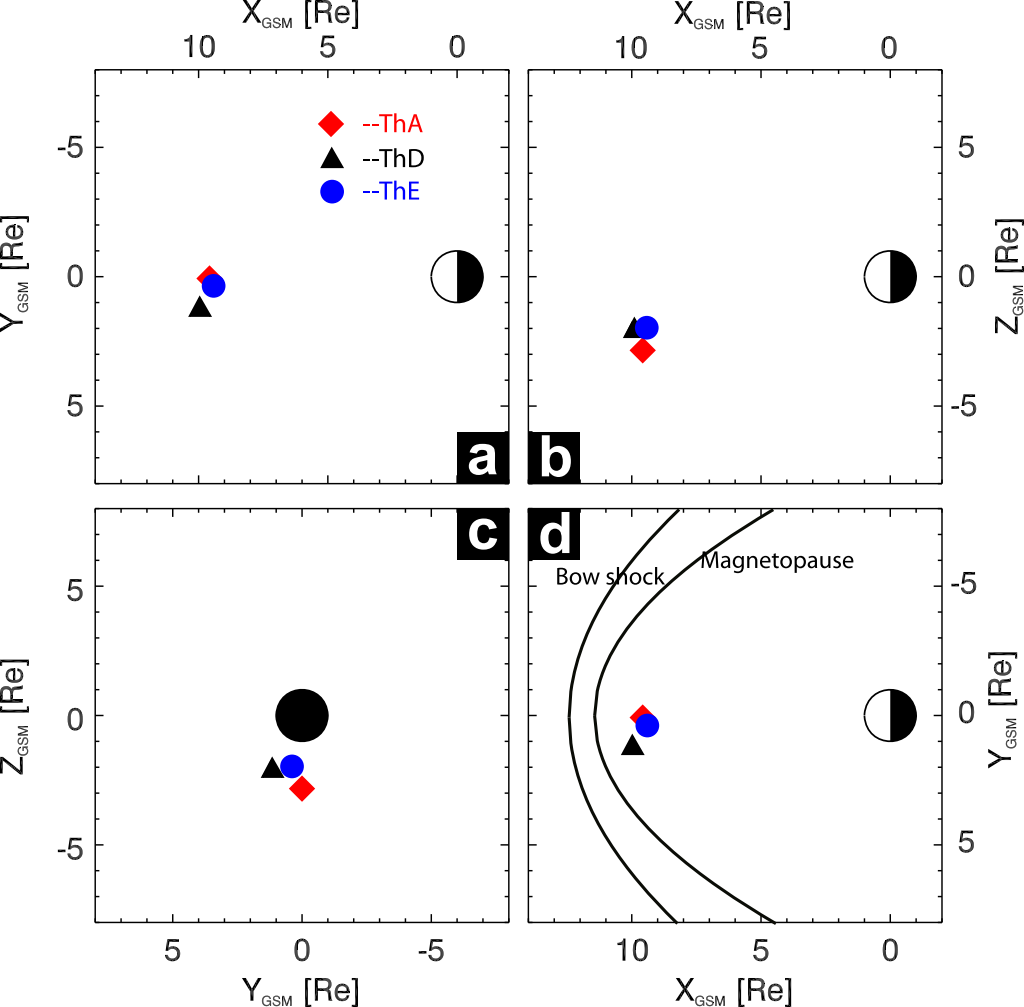
X_GSM [Re]
10
5
0
--ThA
--ThD
--ThE
Y_GSM [Re]
-5
0
5
a
b
c
d
Z_GSM [Re]
Bow shock
Magnetopause
X_GSM [Re]
Y_GSM [Re]
Z_GSM [Re]

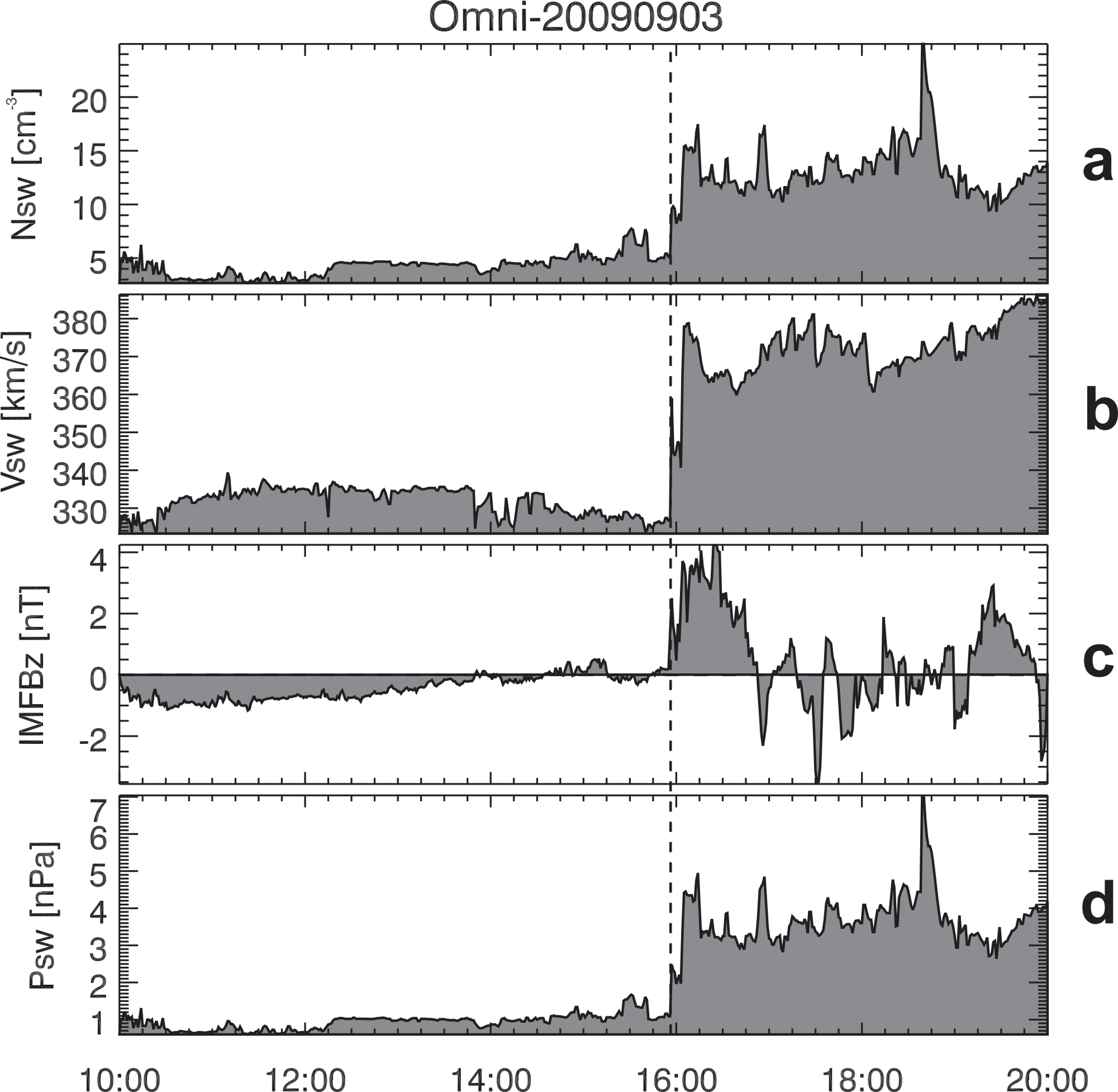
Omni-20090903
Nsw [cm-3]
20
15
10
5
a
Vsw [km/s]
380
370
360
350
340
330
b
IMFBz [nT]
4
2
0
-2
c
Psw [nPa]
7
6
5
4
3
2
1
d
10:00
12:00
14:00
16:00
18:00
20:00

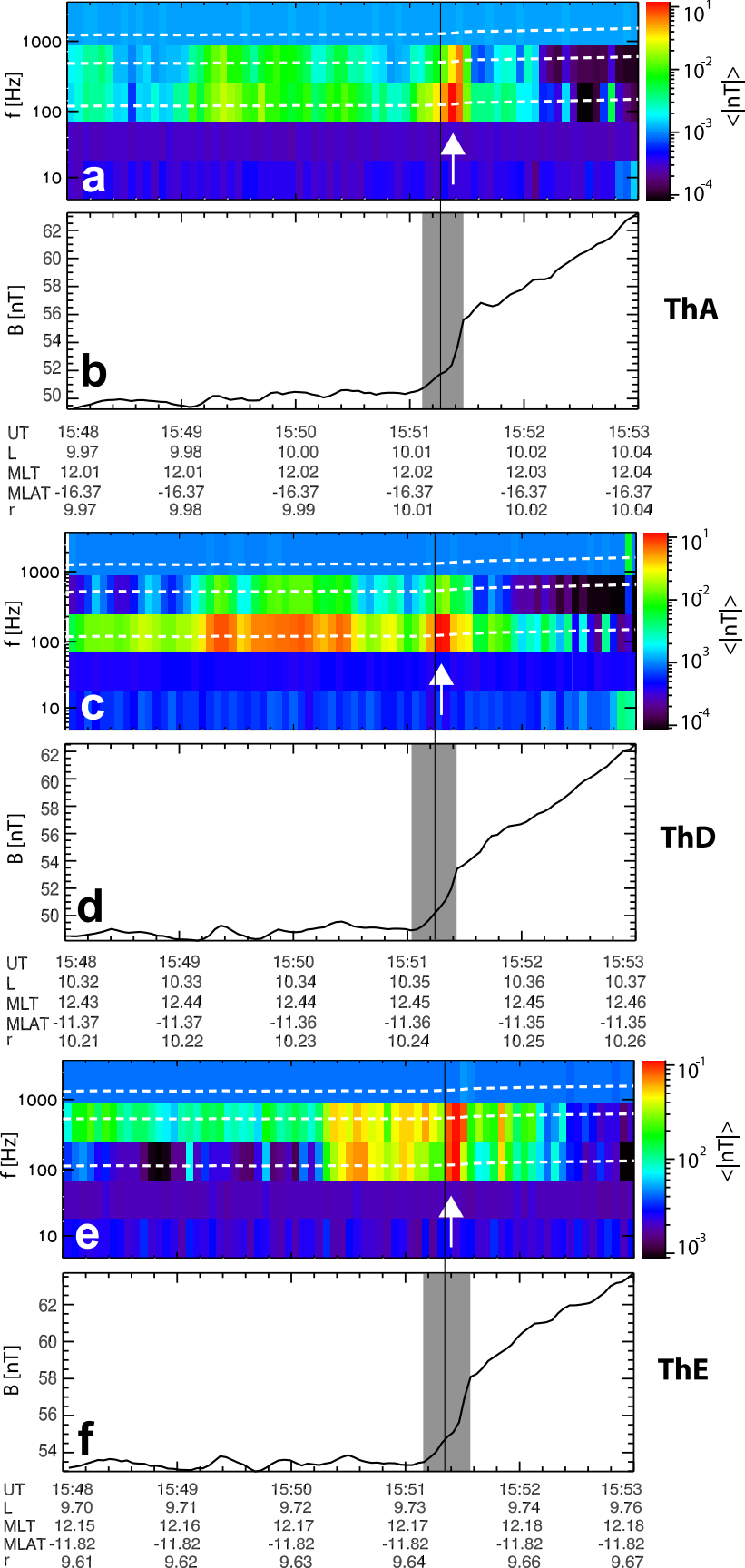
f [Hz]
1000
100
10
a
10^{-1}
10^{-2}
10^{-3}
10^{-4}
<|nT|>
B [nT]
62
60
58
56
54
52
50
b
ThA
UT 15:48 15:49 15:50 15:51 15:52 15:53
L 9.97 9.98 10.00 10.01 10.02 10.04
MLT 12.01 12.01 12.02 12.02 12.03 12.04
MLAT -16.37 -16.37 -16.37 -16.37 -16.37 -16.37
r 9.97 9.98 9.99 10.01 10.02 10.04
f [Hz]
1000
100
10
c
10^{-1}
10^{-2}
10^{-3}
10^{-4}
<|nT|>
B [nT]
62
60
58
56
54
52
50
d
ThD
UT 15:48 15:49 15:50 15:51 15:52 15:53
L 10.32 10.33 10.34 10.35 10.36 10.37
MLT 12.43 12.44 12.44 12.45 12.45 12.46
MLAT -11.37 -11.37 -11.36 -11.36 -11.35 -11.35
r 10.21 10.22 10.23 10.24 10.25 10.26
f [Hz]
1000
100
10
e
10^{-1}
10^{-2}
10^{-3}
<|nT|>
B [nT]
62
60
58
56
54
f
ThE
UT 15:48 15:49 15:50 15:51 15:52 15:53
L 9.70 9.71 9.72 9.73 9.74 9.76
MLT 12.15 12.16 12.17 12.17 12.18 12.18
MLAT -11.82 -11.82 -11.82 -11.82 -11.82 -11.82
r 9.61 9.62 9.63 9.64 9.66 9.67

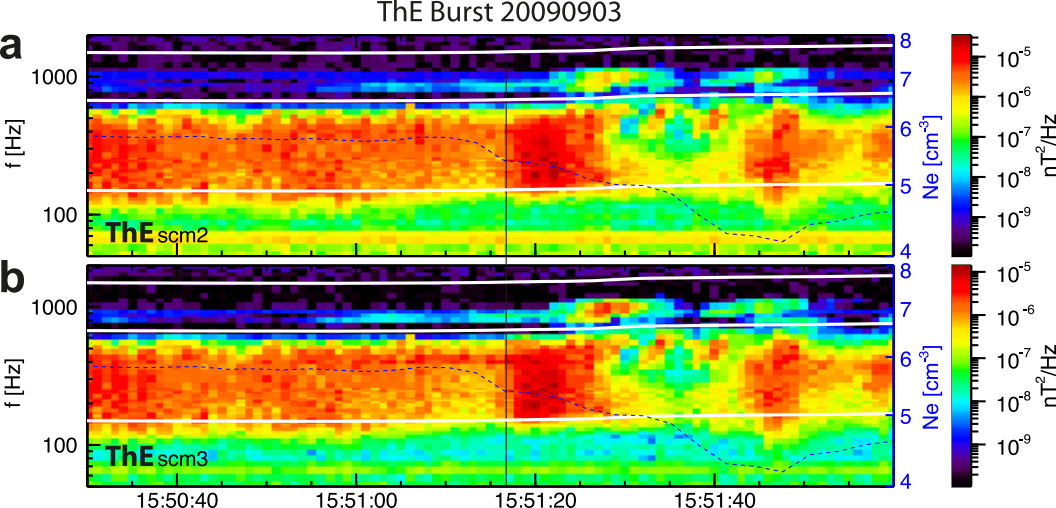
ThE Burst 20090903
a
b
f [Hz]
1000
100
ThE scm2
ThE scm3
Ne [cm^{-3}]
8
7
6
5
4
nT^2/Hz
10^{-5}
10^{-6}
10^{-7}
10^{-8}
10^{-9}
15:50:40
15:51:00
15:51:20
15:51:40

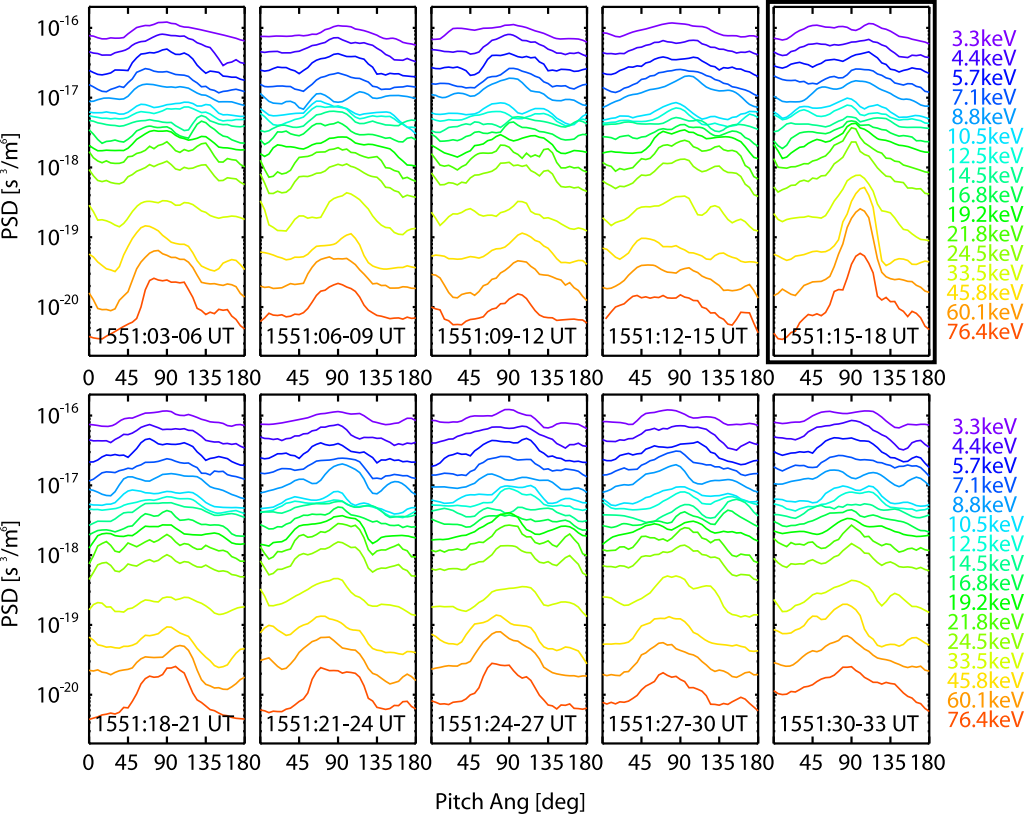
PSD [s^{-3}/m^6]
10^{-16}
10^{-17}
10^{-18}
10^{-19}
10^{-20}
1551:03-06 UT
1551:06-09 UT
1551:09-12 UT
1551:12-15 UT
1551:15-18 UT
1551:18-21 UT
1551:21-24 UT
1551:24-27 UT
1551:27-30 UT
1551:30-33 UT
0 45 90 135 180
3.3keV
4.4keV
5.7keV
7.1keV
8.8keV
10.5keV
12.5keV
14.5keV
16.8keV
19.2keV
21.8keV
24.5keV
33.5keV
45.8keV
60.1keV
76.4keV
Pitch Ang [deg]

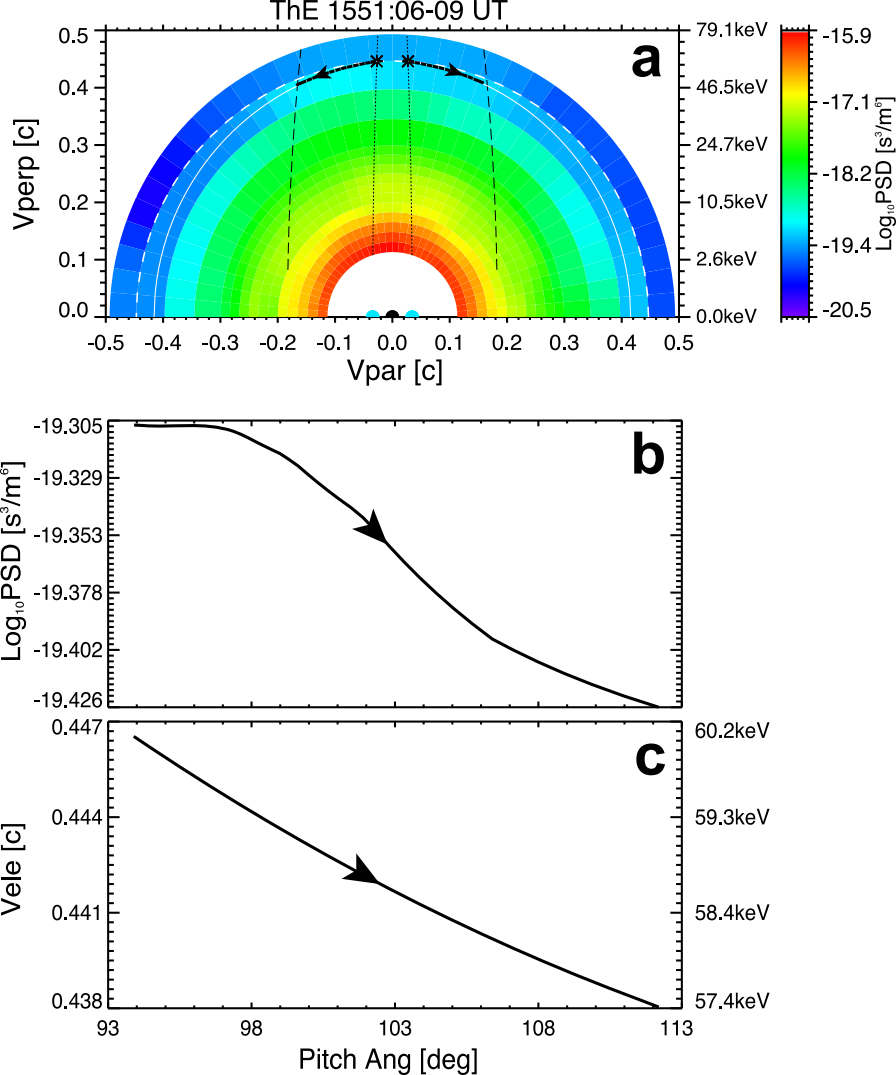
ThE 1551:06-09 UT
a
Vperp [c]
Vpar [c]
0.5
0.4
0.3
0.2
0.1
0.0
-0.5
-0.4
-0.3
-0.2
-0.1
0.0
0.1
0.2
0.3
0.4
0.5
79.1keV
46.5keV
24.7keV
10.5keV
2.6keV
0.0keV
-15.9
-17.1
-18.2
-19.4
-20.5
Log10PSD [s3/m6]
b
Log10PSD [s3/m6]
-19.305
-19.329
-19.353
-19.378
-19.402
-19.426
c
Vele [c]
0.447
0.444
0.441
0.438
60.2keV
59.3keV
58.4keV
57.4keV
93
98
103
108
113
Pitch Ang [deg]

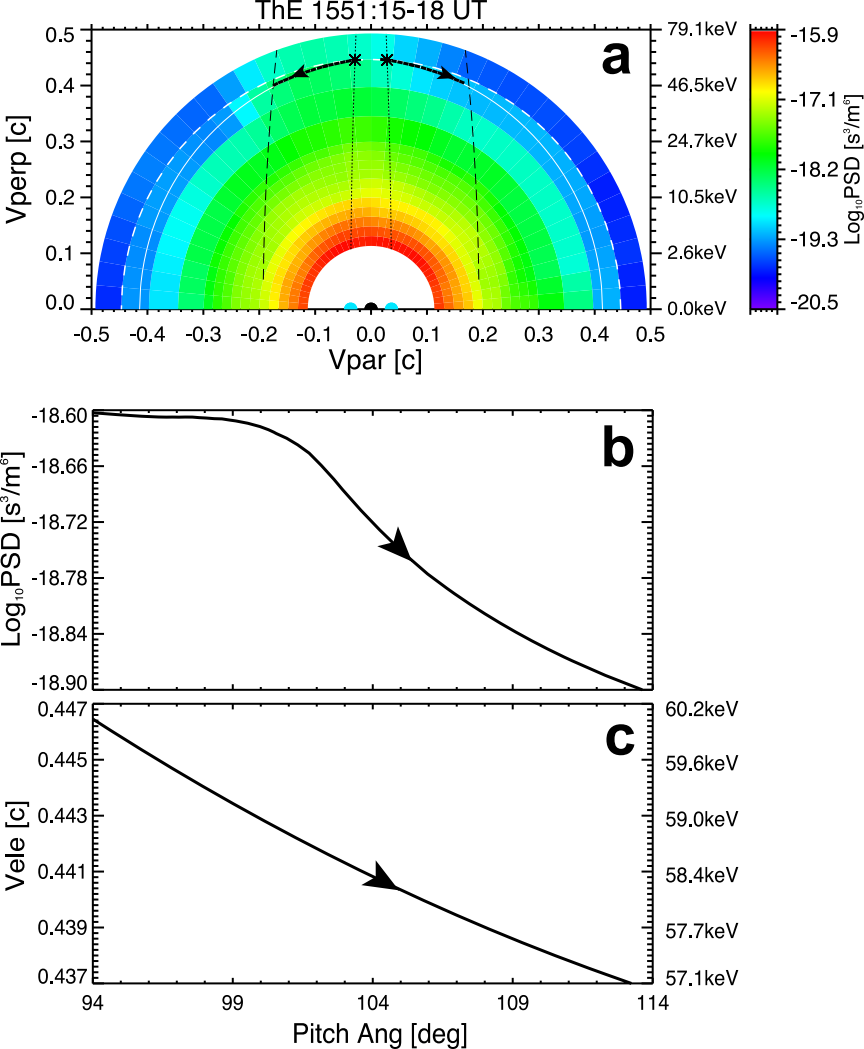
ThE 1551:15-18 UT
a
Vperp [c]
Vpar [c]
79.1keV
46.5keV
24.7keV
10.5keV
2.6keV
0.0keV
Log10PSD [s3/m6]
b
c
Vele [c]
Pitch Ang [deg]
60.2keV
59.6keV
59.0keV
58.4keV
57.7keV
57.1keV

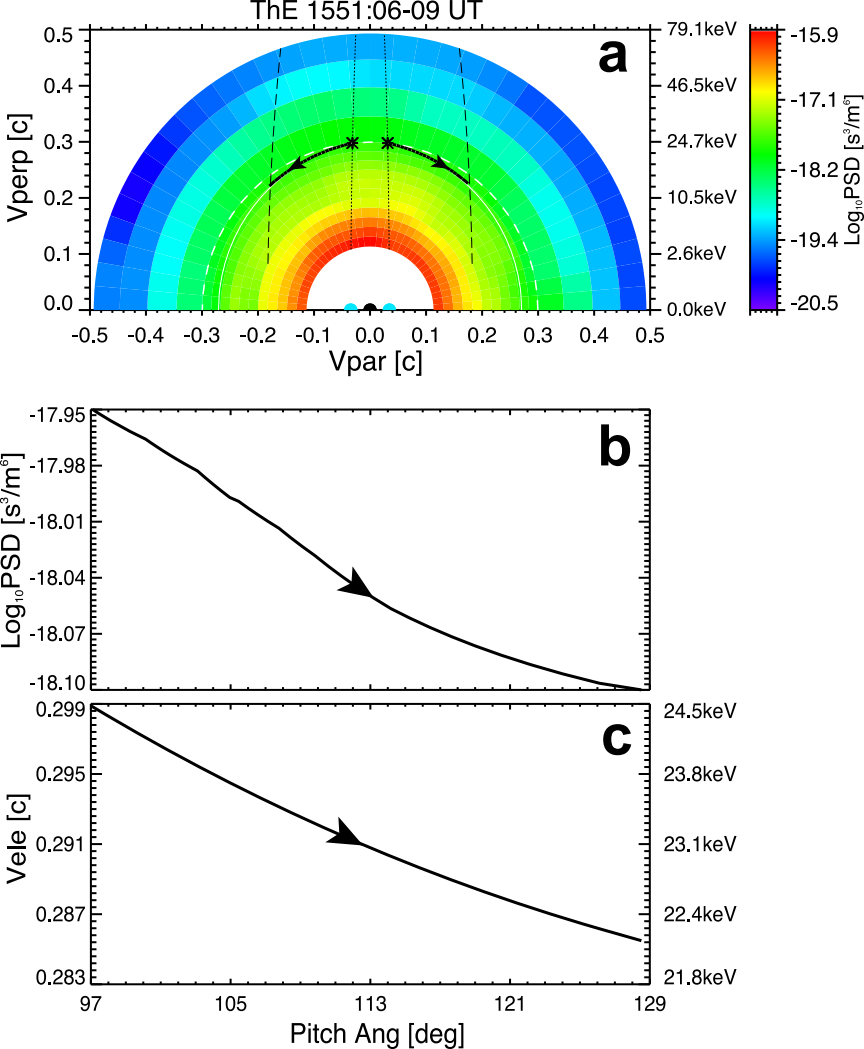
ThE 1551:06-09 UT
a
Vperp [c]
Vpar [c]
79.1keV
46.5keV
24.7keV
10.5keV
2.6keV
0.0keV
Log10PSD [s3/m6]
b
c
Vele [c]
Pitch Ang [deg]
24.5keV
23.8keV
23.1keV
22.4keV
21.8keV

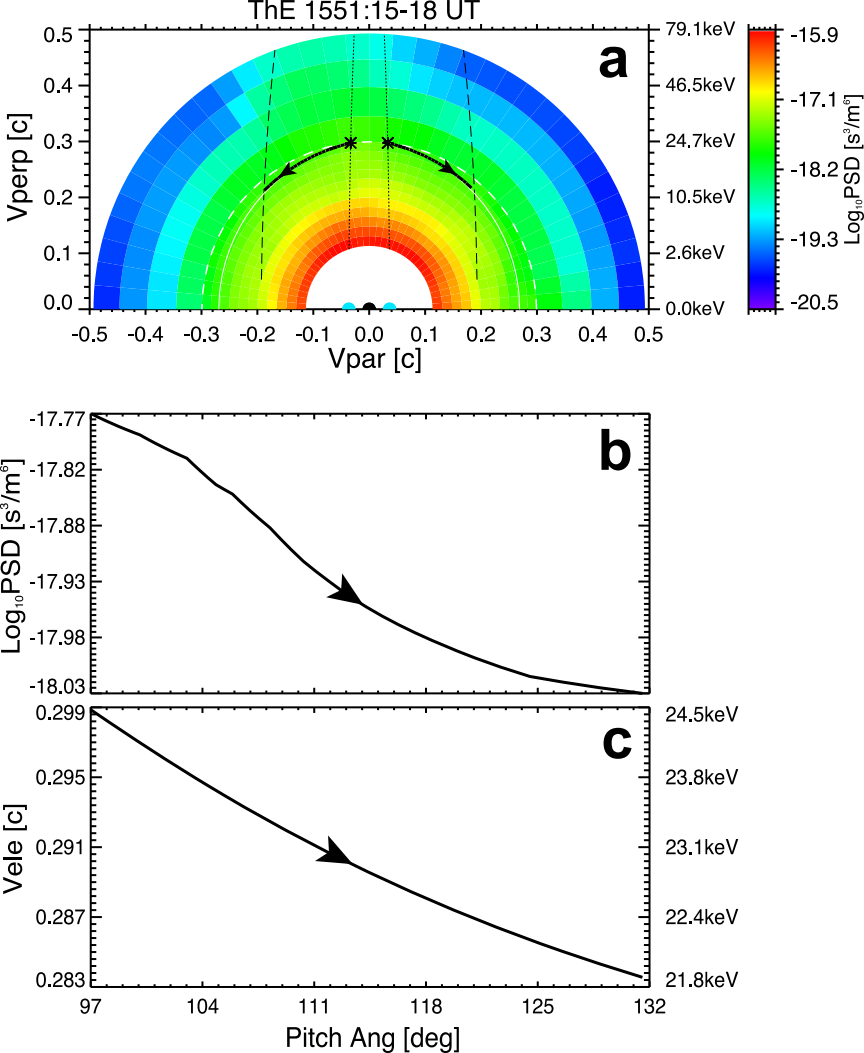
ThE 1551:15-18 UT
a
Vperp [c]
Vpar [c]
79.1keV
46.5keV
24.7keV
10.5keV
2.6keV
0.0keV
Log10PSD [s3/m6]
b
Log10PSD [s3/m6]
c
Vele [c]
24.5keV
23.8keV
23.1keV
22.4keV
21.8keV
Pitch Ang [deg]

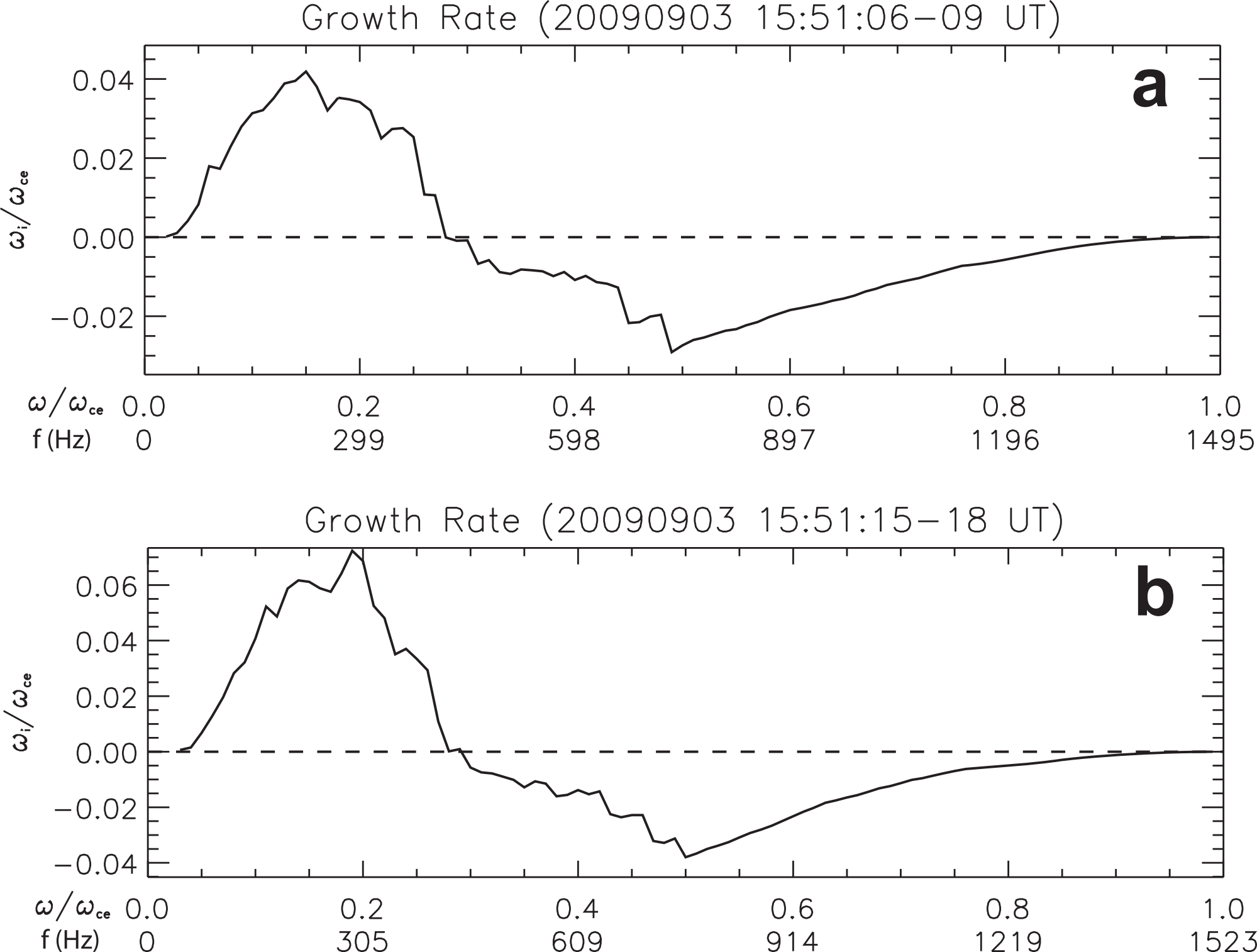
Growth Rate (20090903 15:51:06–09 UT)
a
0.04
0.02
0.00
−0.02
ω_i/ω_{ce}
ω/ω_{ce} 0.0 0.2 0.4 0.6 0.8 1.0
f (Hz) 0 299 598 897 1196 1495
Growth Rate (20090903 15:51:15–18 UT)
b
0.06
0.04
0.02
0.00
−0.02
−0.04
ω_i/ω_{ce}
ω/ω_{ce} 0.0 0.2 0.4 0.6 0.8 1.0
f (Hz) 0 305 609 914 1219 1523

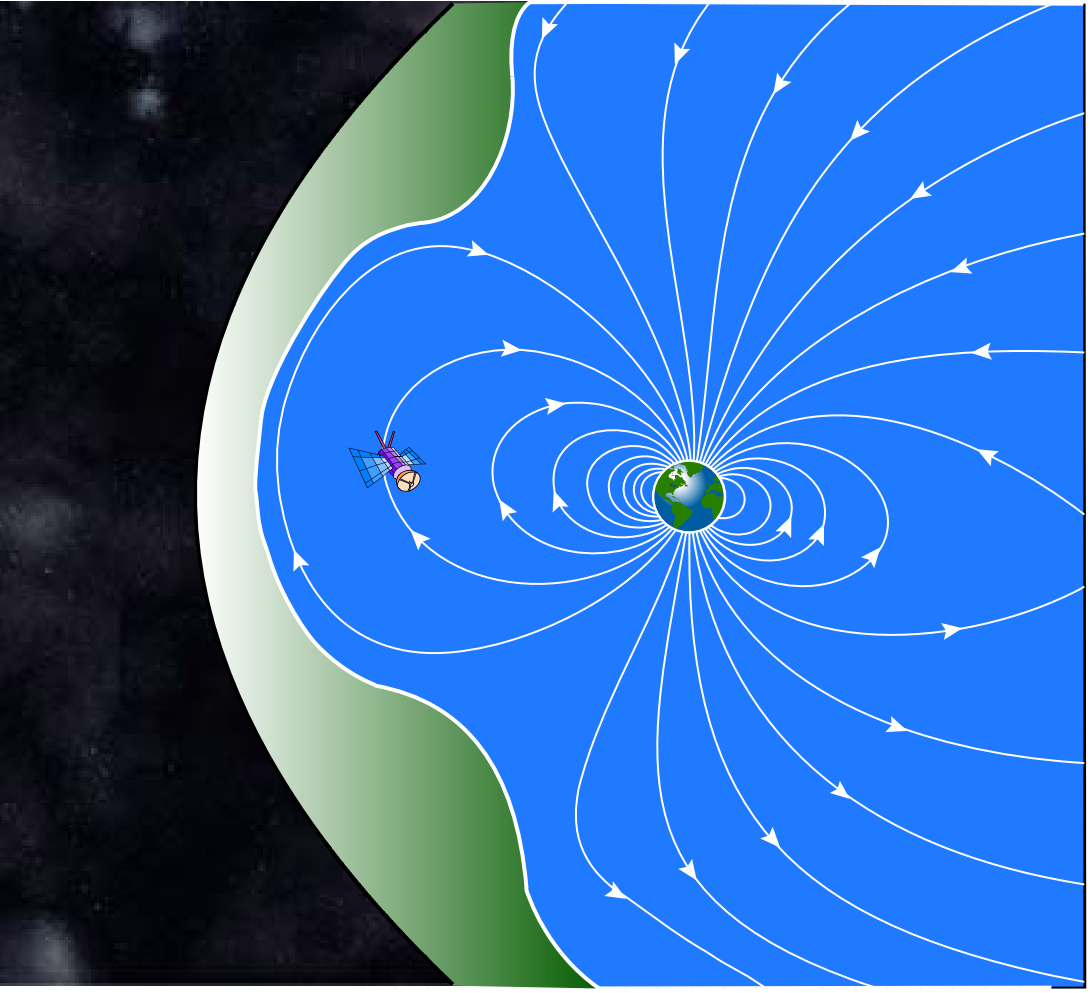

Before Shock

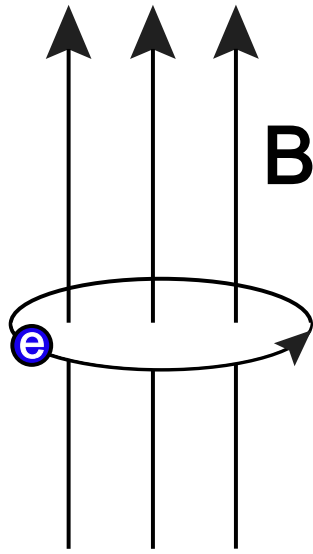

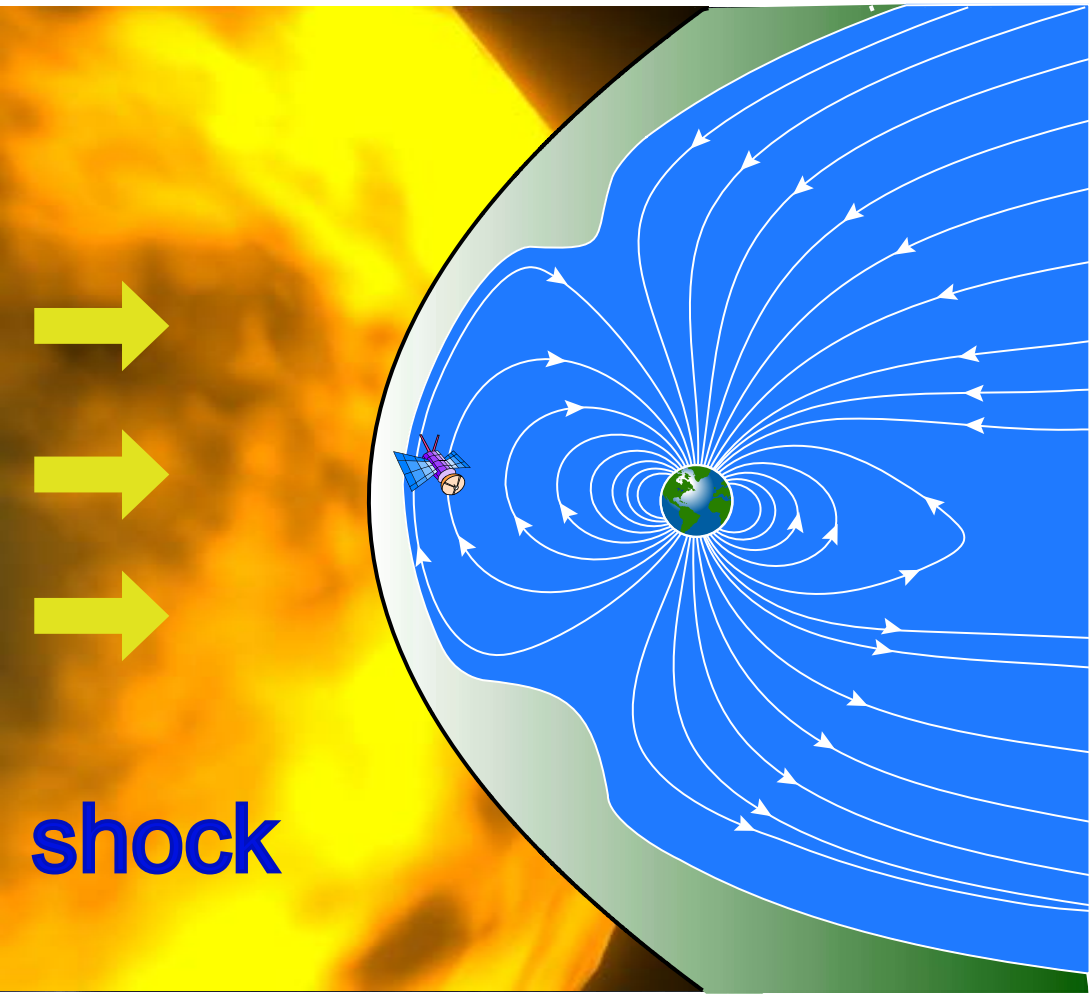

After Shock

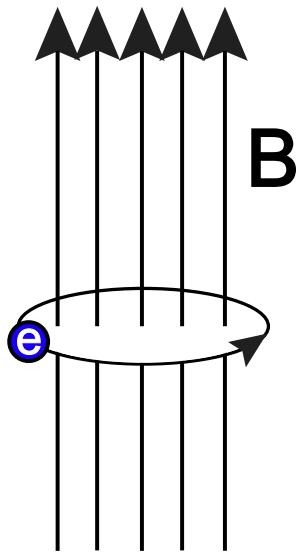

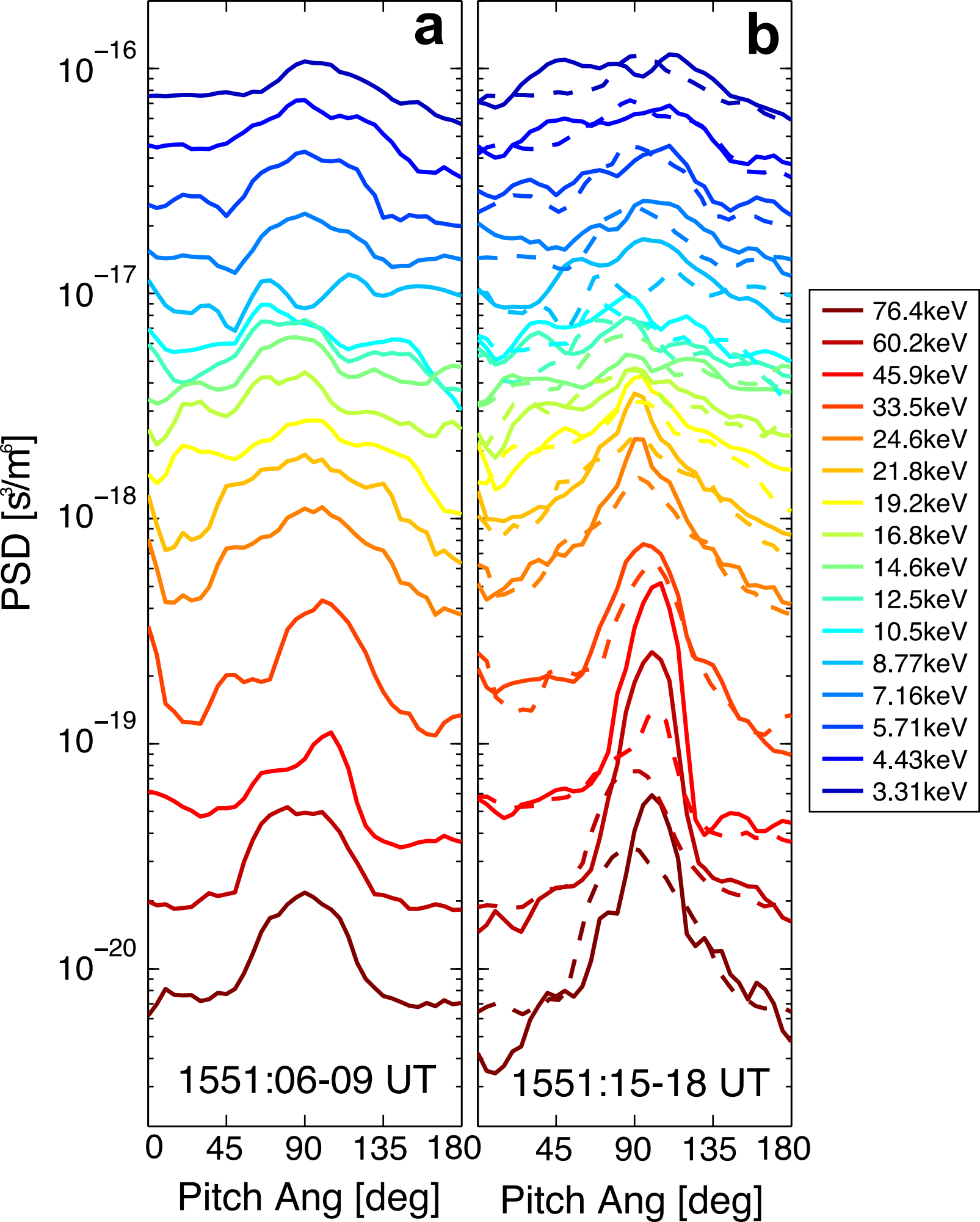
a
b
10^{-16}
10^{-17}
10^{-18}
10^{-19}
10^{-20}
PSD [s^3/m^6]
76.4keV
60.2keV
45.9keV
33.5keV
24.6keV
21.8keV
19.2keV
16.8keV
14.6keV
12.5keV
10.5keV
8.77keV
7.16keV
5.71keV
4.43keV
3.31keV
1551:06-09 UT
1551:15-18 UT
0
45
90
135
180
45
90
135
180
Pitch Ang [deg]
Pitch Ang [deg]

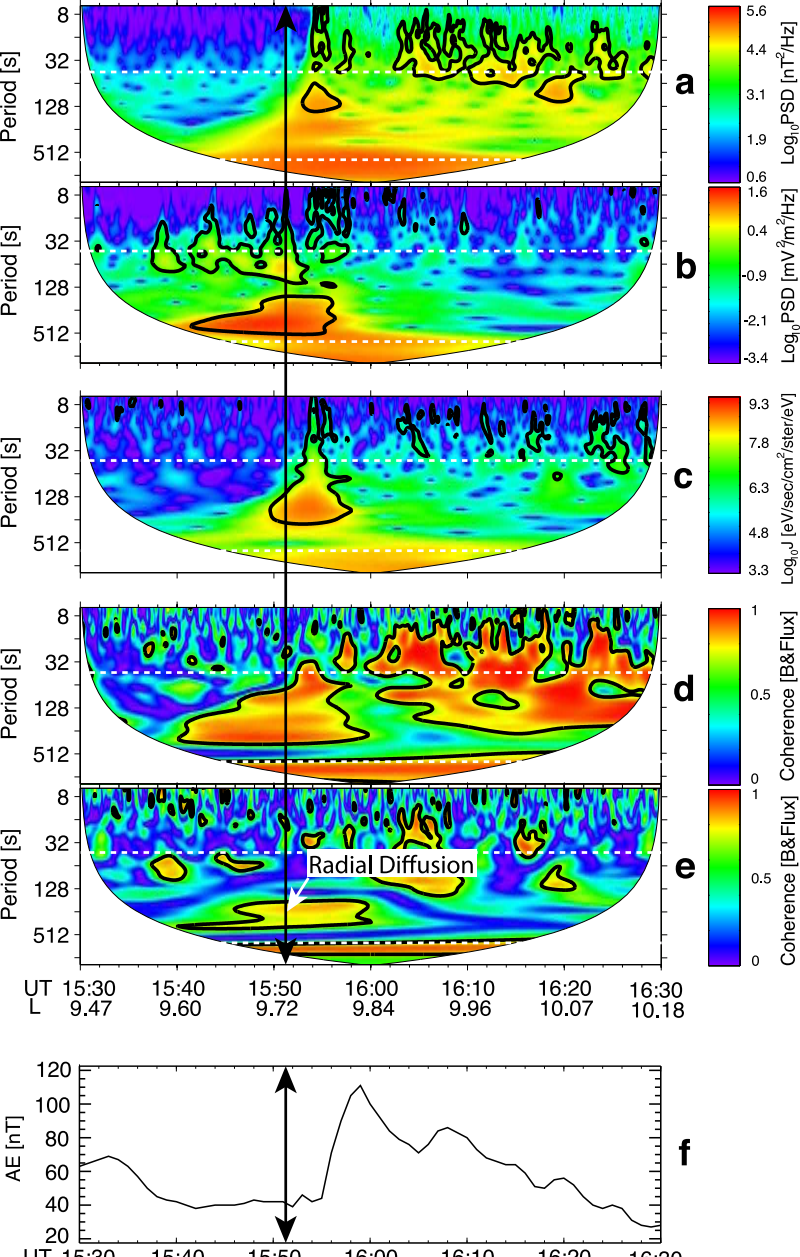
a
b
c
d
e
f
Period [s]
8
32
128
512
Log10PSD [nT²/Hz]
5.6
4.4
3.1
1.9
0.6
Log10PSD [mV²/m²/Hz]
1.6
0.4
-0.9
-2.1
-3.4
Log10J [eV/sec/cm²/ster/eV]
9.3
7.8
6.3
4.8
3.3
Coherence [B&Flux]
1
0.5
0
Radial Diffusion
UT 15:30 15:40 15:50 16:00 16:10 16:20 16:30
L 9.47 9.60 9.72 9.84 9.96 10.07 10.18
AE [nT]
120
100
80
60
40
20